DNA Gold Nanoparticle Motors Demonstrate Processive Motion with Bursts of Speed Up to 50 nm Per Second

Alisina Bazrafshan[1], Maria-Eleni Kyriazi[2], Brandon Alexander Holt[3], Wenxiao Deng[1], Selma Piranej[1], Hanquan Su[1], Yuesong Hu[1], Afaf H. El-Sagheer[4,5], Tom Brown[4], Gabriel A. Kwong[3], Antonios G. Kanaras[2,6] and Khalid Salaita[1,3]*

[1] Department of Chemistry, Emory University, 1515 Dickey Drive, Atlanta, Georgia, 30322 United States,

[2] School of Physics and Astronomy, Faculty of Engineering and Physical Sciences, University of Southampton, Southampton, SO171BJ, U.K.

[3] Wallace H. Coulter Department of Biomedical Engineering, Georgia Institute of Technology and Emory University, Atlanta, Georgia, 30322, United States,

[4] Department of Chemistry, University of Oxford, Chemistry Research Laboratory, 12 Mansfield Road, Oxford, OX1 3TA, U.K.

[5] Chemistry Branch, Department of Science and Mathematics, Faculty of Petroleum and Mining Engineering, Suez University, Suez, 43721, Egypt

[6] Institute for Life Sciences, University of Southampton, Southampton, SO171BJ, U.K.

*Email: k.salaita@emory.edu

Table of contents:

Other Supplementary Materials for this manuscript include the following:

S-I Materials and Methods

A. Synthesis of monomer motors (50 nm DNA-AuNP conjugates)

Modification of 50 nm gold nanoparticles with thiolated DNA was achieved using a recently published method.[1] Briefly, 20 µL of 100 µM thiolated DNA was added to 180 µL of a solution of commercially purchased 50 nm diameter gold nanoparticles from Sigma-Aldrich (Cat # 753645) in DI water in a glass vial. The solution was cooled and frozen by placing it in a –30 °C freezer for 15 min. Subsequently, the 200 µL solution was allowed to thaw at room temperature for 30 min. Freeze-thaw cycles were repeated three times. Then, in order to remove unbound thiolated DNA legs, the solution was centrifuged (5000 rpm for 8 min) and washed with 1 mL of 1X PBS seven times. The resulting modified DNA-AuNPs were stored at 4 °C and used within one week after synthesis.

B. Tuning leg density for nanoparticle motors

To synthesize AuNP DNA nanomotors with tunable density, we created a binary mixture of thiolated polyT and DNA legs oligonucleotides (See **Table S1**). The sum of the concentration of both oligonucleotides was maintained at 10 µM in the final solution. As they were both 30mer polynucleotides, we assumed that the kinetics of binding to the AuNP would be similar. Four different solutions were made to yield four different DNA leg densities (10 µM polyT- 10 µM DNA legs (50%), 5 µM polyT and 15 µM DNA legs (75%), 2 µM poly T and 18 µM DNA legs (90%) and 20 µM DNA legs (100%)). The 20 µL solution was added to 180 µL solution of commercially purchased 50 nm diameter gold nanoparticles in DI water.

C. Preparation of dimer motors

C1. Synthesis of gold nanoparticles for dimer motors. Spherical AuNPs with an average size of 49 ± 0.4 nm (TEM) were synthesized according to a protocol by Bastus *et al.*[2] Briefly a solution of sodium citrate in nanopure water (2.2 nM, 150 mL) was heated to boiling point in a 3-neck round bottom flask fitted with a condenser. $HAuCl_4$ (25 mM, 1 mL) was then injected into the solution and a color change to light pink was observed. Immediately after, the solution was cooled to 90 °C after which sodium citrate (60 mM, 1 mL) and $HAuCl_4$ (25 mM, 1 mL) were sequentially injected into the solution (time delay of 2 min between additions). The solution was then allowed to stir at 90 °C for 30 min. The addition process was repeated twice resulting in generation 1 (G1) AuNPs. The sample was then diluted by extracting 55 mL and adding nanopure water (53 mL) and sodium citrate (60 mM, 2 mL). This was then used as the seed solution and the process was repeated until generation 5 (G5) AuNPs were obtained. Resulting AuNPs were then purified by centrifugation (5000 rpm, 20 min), redispersed in citrate buffer and stored at 4 °C until further use.

C2. DNA modification of nanoparticles (for dimer motors). The surface of spherical AuNPs was functionalized with synthetic oligonucleotides using a modified freeze/thaw approach.[3] Initially, two separate batches of synthesized 49 ± 0.4 nm AuNPs (50 pM, 900 µL) were centrifuged at 6000 rpm for 10 minutes and diluted 5-fold by discarding 720 µL of the supernatant. To create DNA-nanoparticle batch 1, AuNP (250 pM, 180 µL) were mixed with DNA leg oligonucleotides (100 µM, 20 µL) and DNA linker strand 1 (45 nM, 1 µL, 1:1 molar ratio between linker strand and AuNPs) were mixed together. DNA nanoparticle batch 2 was synthesized using an identical protocol but using DNA linker strand 2 (rather than DNA linker strand 1). The vials

were put in the freezer (for 15 min) and thawed three times. After the last thaw, the functionalized AuNPs were washed *via* three rounds of centrifugation (6000 rmp, 20 min) and finally re-dispersed in PBS buffer.

C3. Covalent conjugation of DNA-nanoparticle conjugates to generate motor dimers. Following oligonucleotide functionalization, batch 1 and batch 2 of oligonucleotide – coated 49 ± 0.4 nm AuNPs were combined at an equimolar ratio to allow for hybridization to take place between DNA linker strand 1 of batch 1 and DNA linker strand 2 of batch 2. The solution was heated up to 75 °C for 5 min followed by slow cooling to room temperature. Resulting dimers were purified by one round of centrifugation (5000 rpm, 20 min) and re-dispersed in PBS buffer.

D. Quantification of the number of DNA legs per motor

The DNA legs were labelled with FAM fluorescein fluorophore. This modification was used to quantify the number of DNA legs per particle. A calibration curve with concentrations of 0, 4, 16, 64, 128 and 256 nM DNA legs was prepared at a final volume of 100 µL in 1× TE buffer. DNA solutions were prepared by diluting a 10 nM stock of motor particles to 40 pM. The DNA legs were then released from the particles by oxidizing/dissolving the gold with potassium cyanide (KCN). This was performed by adding 1 µL of a 5 M stock solution of KCN to each well, including the calibration wells to ensure an accurate calibration curve and blank subtraction. The samples were incubated with KCN for 30 min to ensure complete dissolution. Complete dissolution is assumed by observing the transparent solution after addition of KCN, the 30-minute reaction time and the 10 order of magnitude excess of KCN in solution. After complete dissolution of the gold nanoparticles, fluorescence intensities (485/528 nm excitation/emission) of each well were then measured using a BioTek Synergy plate reader to determine the total DNA density. By dividing the concentration of DNA legs in solution by the concentration of 50 nm AuNP (read by a nanodrop at $\lambda_{max} = 535$) the number of DNA legs per motor was determined.

E. Transmission Electron Microscopy

TEM images were collected using a Hitachi HT-770 microscope operating at 80kV with magnification between 15,000x and 70,000x. Images were binarized using imageJ software. Binarized images were analyze using built-in particle analyzer plugin to extract particle radii.

F. RNA monolayer preparation

RNA monolayer preparation was performed following previously published protocols[4]. Briefly, a #1.5 glass slide (25 × 75 mm) was cleaned by sonication in DI water for 15 minutes. The sample was then subjected to a second sonication in 200 proof ethanol for 15 minutes and was subsequently dried under a stream of N_2. The glass slide was etched by piranha solution (v/v = 3:7 hydrogen peroxide/sulfuric acid, please take caution as piranha is extremely corrosive and may explode if exposed to organics) for 30 min to remove residual organic materials and activate hydroxyl groups on the glass. The cleaned substrates were rinsed with DI water in a 200 mL beaker 6 times and further washed with ethanol thrice. Slides were then transferred to a 200 mL beaker containing 2% (v/v) APTES in ethanol for 1 h, washed with ethanol thrice and thermally cured in an oven (~110ºC) for 10 min. The slides were then mounted to 6-channel microfluidic cells (Sticky-Slide VI 0.4, Ibidi). To each channel, ~50 µL of 10 mg/mL of NHS-PEG$_4$-azide (Click Chemistry Tools) in 0.1 M NaHCO$_3$ (pH = 9) was added and incubated for

2h. The channels were washed with 1 mL DI water thrice and the remaining water in the channels was removed by pipetting. After thoroughly rinsing the surface with DI water, a solution of 10 µM alkyne modified DNA (anchor strand), 50 µM THTPA, 10 µM CuSO4 and 1 mM sodium ascorbate in 1 M potassium phosphate buffer was added to the surface and incubated for 1 hour. After incubation, excess DNA was removed from the channel using a ~5 ml DI water rinse. Lastly, the RNA substrate was immobilized to the surface through hybridization by adding a 100 µl of a complementary RNA/DNA chimera (100 nM) in 1 × PBS for 12 hours at room temperature. The wells were sealed with Parafilm for each step to prevent evaporation and the resulting RNA monolayer remained stable for weeks, as determined by fluorescence imaging.

G. Optical microscopy

A Nikon Ti Eclipse microscope was used for all widefield imaging of nanomotors. The microscope was equipped with an Intensilight epifluorescence source (Nikon), a CFI Apo 100x NA 1.49 objective (Nikon). The microscope also included a Nikon Perfect Focus System, which allows the capture of multipoint and time-lapse images without loss of focus. FITC and Cy3 images were obtained using the Quad Cube (Product No. 97327) and TRITC (Product No. 96321) filter cube set supplied by Chroma. For time lapse experiments, using the ND acquisition toolbox in the Elements software package, one RICM image with 500 ms exposure time was captured every 5 seconds for 0.2 Hz frame rate. For 2 Hz frame rate, one RICM image with 500 ms exposure time was captured every 500 ms (continuous imaging using the "fast time lapse" add-on). The images were collected at 16-bit depth using an Andor EMCCD iXON DU897 512x512 camera. All imaging was conducted at room temperature.

A Nikon Ti2 microscope was used to capture wide field fluorescence images of depletion tracks after the time lapse to quantify percent fluorescence loss during motor motion and Kuhn segment analyses. This microscope was equipped with SOLA SE Light Engine. and Nikon Perfect Focus System. The images were collected at 16-bit depth using Prime 95B 25mm™ Scientific CMOS 1608x1608 Camera (Photometrix, AZ).

H. RICM tracking and trajectory analyses of 50 nm motors

Time lapses of 50 nm AuNP DNA motors were inverted, then background subtracted using ImageJ (**Figure S7).** The particles (that are now bright because of inversion) were tracked using the MOSAIC tool suite[1]. User defined conditions were as follows: Particle radius: 2 (pixels), intensity percentile: 0.1 (%), Cutoff score: 0.001, maximum step length: 2, link range: 2. The XY trajectories were then transferred to an excel file which was then exported to MATLAB. Using custom MATLAB code along with the MSDanalyzer toolbox[2], we obtained particle trajectories that were drift corrected (**Figure S11**). The drift corrected trajectories were then smoothed and converted into absolute distances by multiplying using our microscope distance/pixel calibration. For reference, our EMCCD camera produced images where 1 pixel = 160 nm. Motor displacement ($d(t)$), net displacement, steps, speed, MSD *vs* lag times, and α values were calculated as described below.

Motor displacement $d(t)$ was calculated using equation 1,

$$d\,(t) = \sqrt{\left(x(t) - x(0)\right)^2 + \left(y(t) - y(0)\right)^2} \quad (1)$$

where $x(0)$ and $y(0)$ represent the particle initial position, and $x(t)$ and $y(t)$ represent the position of the particle at time (t). The position of the particle at each time point was estimated by using its moving average from 3 time points. For these experiments, the time lapse videos were typically collected up to $t = 1800$ s, which was used to calculate the net displacement at the end of the RICM acquisition. The motor net displacement ($d(t=1800s)$) is then defined as the displacement at $t = 1800$ s which is the end of the RICM acquisition.

Motor step is defined as the absolute distance traveled by the motor in one time interval. This was calculated using equation (2), where each time point was typically separated by 5 sec intervals.

$$motor\ step\ (nm) = |d(t_{i+1}) - d(t_i)| \quad (2)$$

Motor speed was calculated by dividing the motor step distance (eqn. 2) by the time interval between consecutive average locations (Δt), as shown in equation 3:

$$motor\ speed\ \left(\frac{nm}{s}\right) = \frac{|d(t_{i+1}) - d(t_i)|}{\Delta t} \quad (3)$$

$\Delta t = 5$ seconds for most of the study unless otherwise noted.

Motor mean squared displacement (MSD) for each lag time (τ) was calculated by,

$$< MSD\ (\tau) > = < \left(d(t + \tau) - d(t)\right)^2 > \quad (4)$$

where $d(t)$ and $d(t + \tau)$ are the positions of a single particle at two time points separated by τ seconds apart.

To determine the α value for each individual track, we fit individual $\log(<MSD(\tau)>)$ vs $\log(\tau)$ plots and the slope yields the power law dependence, α. We calculated the α value using 25% of the $<MSD>$ vs τ curve (450 sec maximum lag time for 1800 sec timelapse videos). The reason for choosing this time window is due to the increased stalling and dissociation at later time points and also because the number of data points available at long lag times is limited and more noisy. The 450 sec max lag time thus provides a more robust fit for the $<MSD>$ vs t plot as shown in **Figure S15**.

I. **Analysis of motor processivity by quantifying bound motor density as a function of time**

The fraction of motors that remained bound as a function of time was calculated with the following steps using an automated MATLAB script. The data sets that were exported using the MOSAIC tool suite includes xy localization for all trajectories. Using this data, we created the following script that performed the following operations: 1. Count the number of trajectories that were present in the first frame of a timelapse. 2. Other trajectories that are not present in the first frame are deleted. 3. Trajectories with lengths lower than 20 are deleted (as it is a residue of inversion of the channel). Steps 1-3 provide data sets that include trajectories that start at frame 1 and have different lengths (all >20 frames). 4. The fraction of motors that remain bound as a

function of time was calculated by dividing the number of trajectories present at each time point by the number of trajectories present at frame 1.

J. Super-resolution imaging (SIM) of the fluorescence-depletion tracks

SIM images were acquired on a Nikon N-SIM system equipped with a CFI Apo 100x 1.49NA objective and an Andor iXon EMCCD (60 nm per pixel). For each N-SIM image, nine images of a 3′-Cy3-RNA sample were acquired in different phases using a 561 nm laser as an excitation source and were reconstructed using the Nikon Elements software package.

K. Computational modeling of DNA motors

In order to model the behavior of the DNA motors, we used a combination of a Monte-Carlo simulation and a Gillespie algorithm. We used features of Monte-Carlo simulations to model the movement in 2 spatial dimensions, as well as to keep track of the state of each DNA, RNA, and enzyme molecule independently. We used features of Gillespie algorithms to capture the stochastic nature of the biological processes involved (*e.g.*, DNA/RNA complexation, enzyme cleavage*, etc*.).

To keep track of the state of all molecules, we created three separate integer arrays for each of the molecule types: DNA, RNA, and enzymes (*i.e*., Monte-Carlo). The enzyme array was a 1D array (*i.e*., list) that simply kept track of the state of individual enzyme molecules, without regard to spatial position. The RNA array was a 2D array, where the relative location of each element in the array represented their physical location in space. The DNA array was also a 2D array, which represented only whichever DNA molecules were currently capable of interacting with the surface (*i.e*., locations on a sphere). For the DNA and RNA arrays, each element could take on three states: 0, 1, or 2. The state-0 meant the molecule was currently unbound, whereas the state-1 meant the molecule was currently bound. For RNA, the state-2 meant that RNA had been cleaved and was therefore removed from the system. For DNA, the state-2 meant that the DNA molecules was absent from the system, which was used to model lower densities.

To calculate the time to complete each event on a single molecule, stochastic level, we modeled the major biological events as Poisson processes (*i.e*., Gillespie algorithm). For example, the complexation of an RNA and DNA molecule is a probabilistic event, which can be represented by the kinetic constant, k_{on}. In a Poisson process, we can use an exponential distribution to calculate the wait time between events, where the inverse of the kinetics constant (*i.e*., k_{on}) is the mean of the distribution. This same calculation can be made for the unbinding of a DNA-RNA complex (*i.e*., k_{off}), and enzymatic cleavage (*i.e*., k_{cat}). All of these constants used in the model were estimated from experimental measurements ($k_{on} = 1$, $k_{off} = 3$, $k_{cat} = 3$ s^{-1}).[4]

The model used a discrete iteration to loop through time, with a variable to control the time-step size (*i.e*., lower step sizes resulted in higher resolution, but longer run-times). At each time step, the algorithm looped through each element of all three arrays to update the state and progress of each molecule. The progress was represented by a second array of each type to store the amount of time remaining for the process at each position. For each element, there were four conditional possibilities: (1) If there was an operation in progress, the size of the time-step would be subtracted from the progress, and if the result was less than 0, the process would be completed,

and the state would be updated. (2) Otherwise, if the DNA and RNA molecules in closest proximity are both in the unbound state (*i.e*., state-0), then they will begin binding. (3) If the DNA and RNA molecules are both in the bound state (*i.e*., state-1), then they can either begin unbinding, or begin being cleaved by an open enzyme. (4) If either the DNA or RNA molecules are missing (*i.e*., state-2), then nothing occurs.

After the state of each element in all three arrays has been updated, the algorithm checks for lifting (dissociation), which occurs when all DNA molecules are simultaneously unbound from the surface (*i.e.,* all in state-0). If no lifting has occurred, then the time and position of the particle are updated, and the next iteration begins. To update the position, the model checks the number of consecutive edge-adjacent rows that are completely unbound (*i.e*., state = 0). The model then chooses a number of position units to move in the x and y directions with a uniform distribution using the number of consecutive cleared rows on opposing edges as minimums and maximums.

The DNA array is designed in a way that when only the bottom row of DNA completely unbinds (all values have state = 0), the particle is permitted to roll forward. If this happens, the bottom row is no longer part of the surface of the sphere capable of binding RNA, and therefore leaves the system. During the same timestep, a new row of unbound DNA (top row) becomes available to bind RNA and enters the system. In the model, the bottom row was deleted from the DNA array and a new row was added to the top. Thus, the DNA array allows for rolling. The array maintains a constant area but is now representing a slightly shifted area on the sphere's surface.

During this step, the position of the motor is also updated. Since the particle moved forward by an average distance of the space between two consecutive rows of DNA on the particle surface, the model adjusts the Y position of the particle by this amount. (Note: this means the distance scale in the model is driven by the space between DNA molecules on the particle surface, which is experimentally measurable). If multiple rows are unbound during the same timestep, then the particle may move in integer-multiples of the distance between DNA molecules on the particle surface.
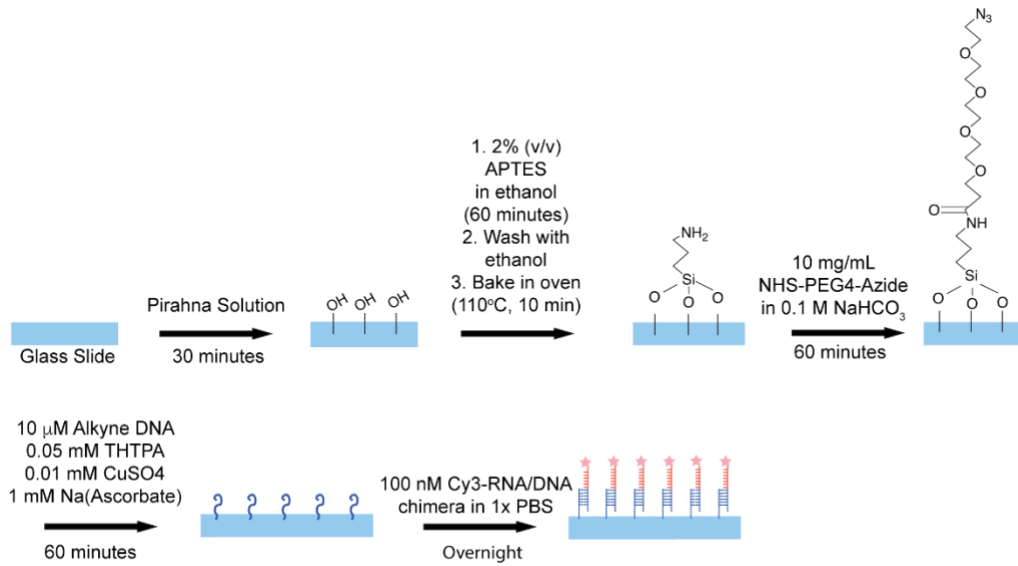
Figure S1. Schematic of the surface preparation steps used for preparing RNA monolayer surfaces. The red color indicates RNA sequence, while blue indicates DNA. Surface preparation is similar to that reported in our previous work.[4]
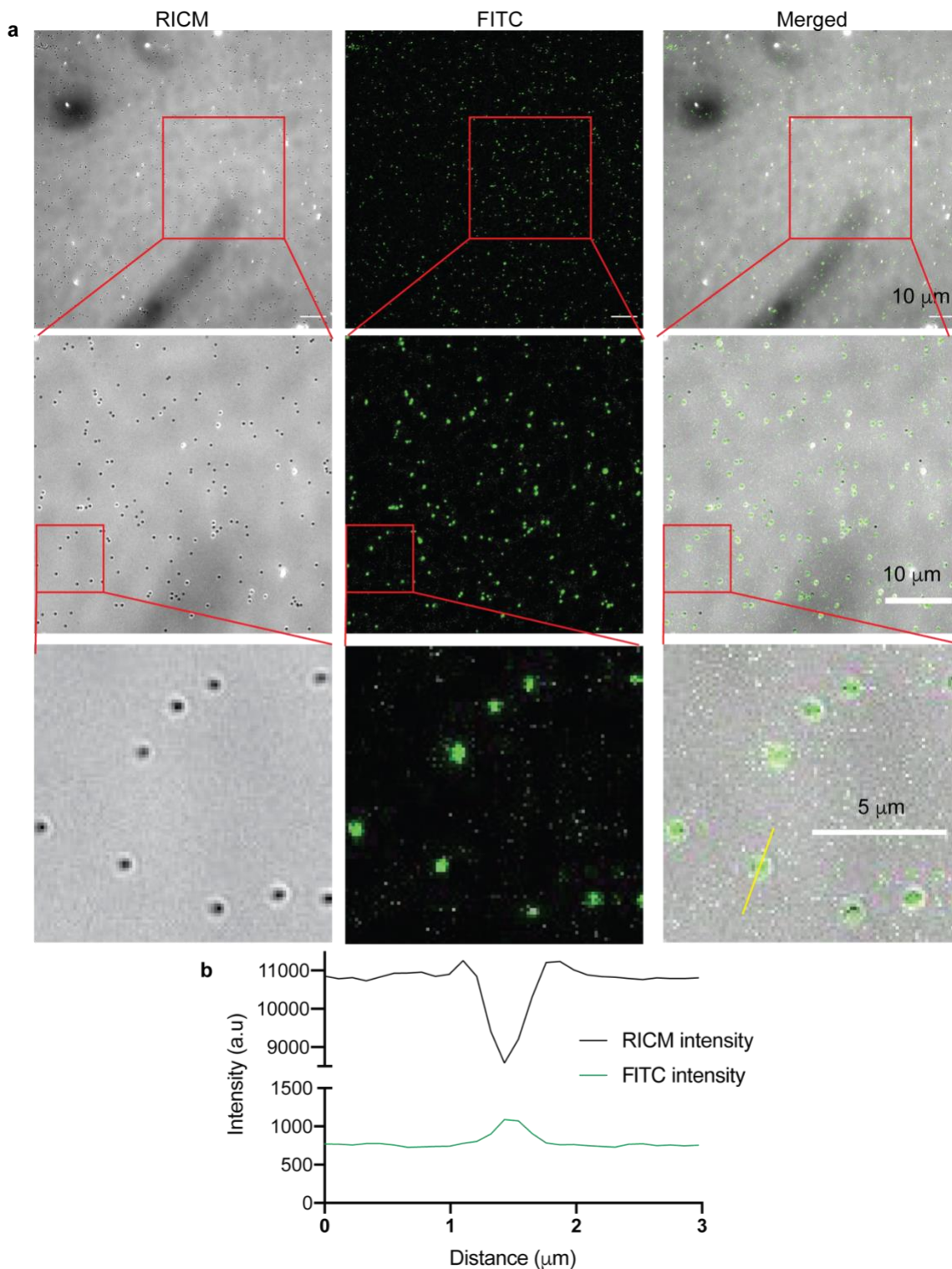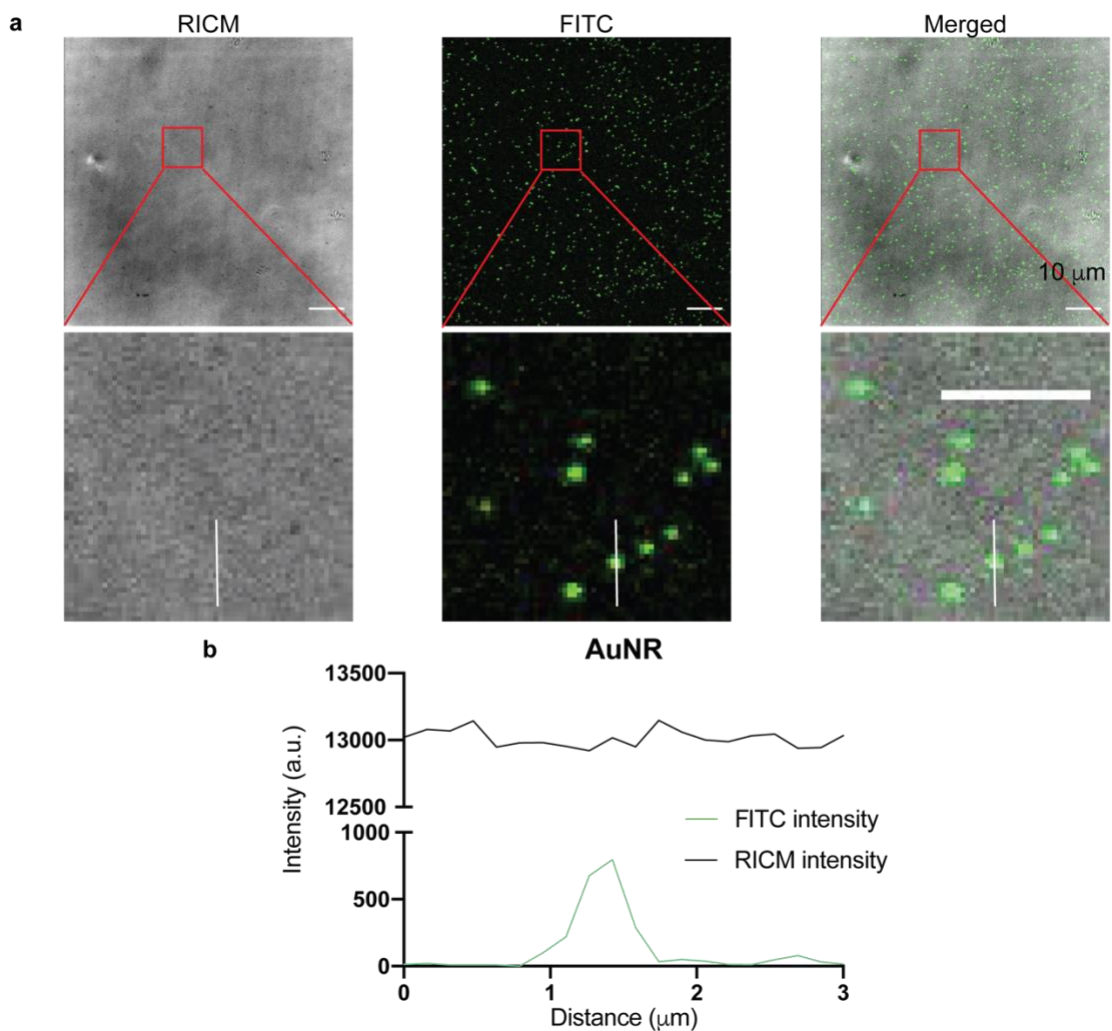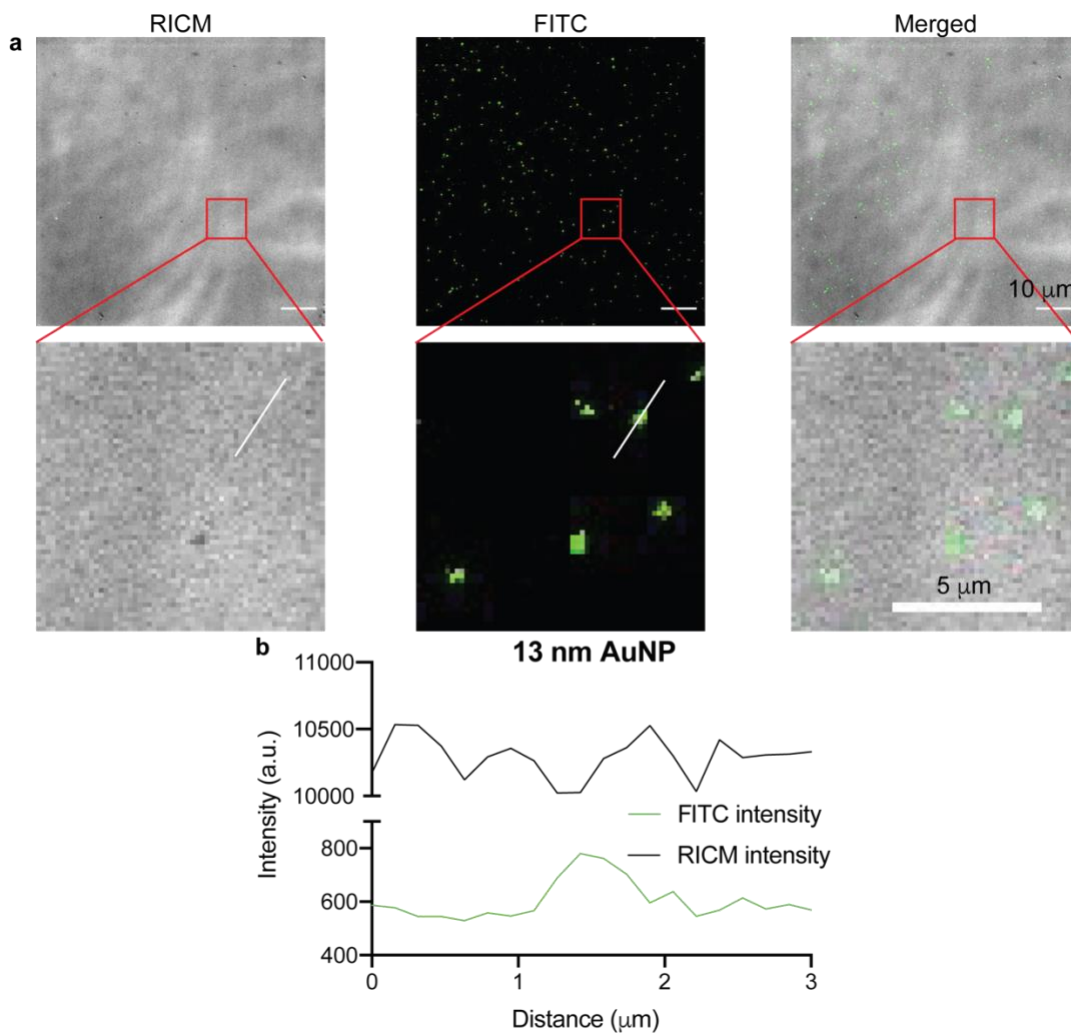
Figure S2. Imaging of 50 nm DNA-AuNPs bound to the RNA monolayer in FITC and RICM channels. (a) Representative RICM, FITC channel images and overlay of 50 nm particles on RNA monolayer. (b) A linescan of a 50 nm DNA-AuNPs in two channels, showing intensity profile in RICM and FITC channels.

Figure S3. Imaging of 10x40 AuNRs bound to the RNA monolayer in FITC and RICM channels. (a) Representative RICM, FITC channel images and overlay of 10x40 AuNRs on RNA monolayer. **(b)** A linescan of a single AuNRs shows the profile in FITC channel. Note that these particles are not detected in RICM.

Figure S4. Imaging of 13 nm AuNPs bound to the RNA monolayer in FITC and RICM channels. (a) Representative RICM, FITC channel images and overlay of 13 nm AuNPs on RNA monolayer. **(b)** A linescan of a single AuNP in two channels showing 13 nm AuNPs fail to provide sufficient signal in RICM.
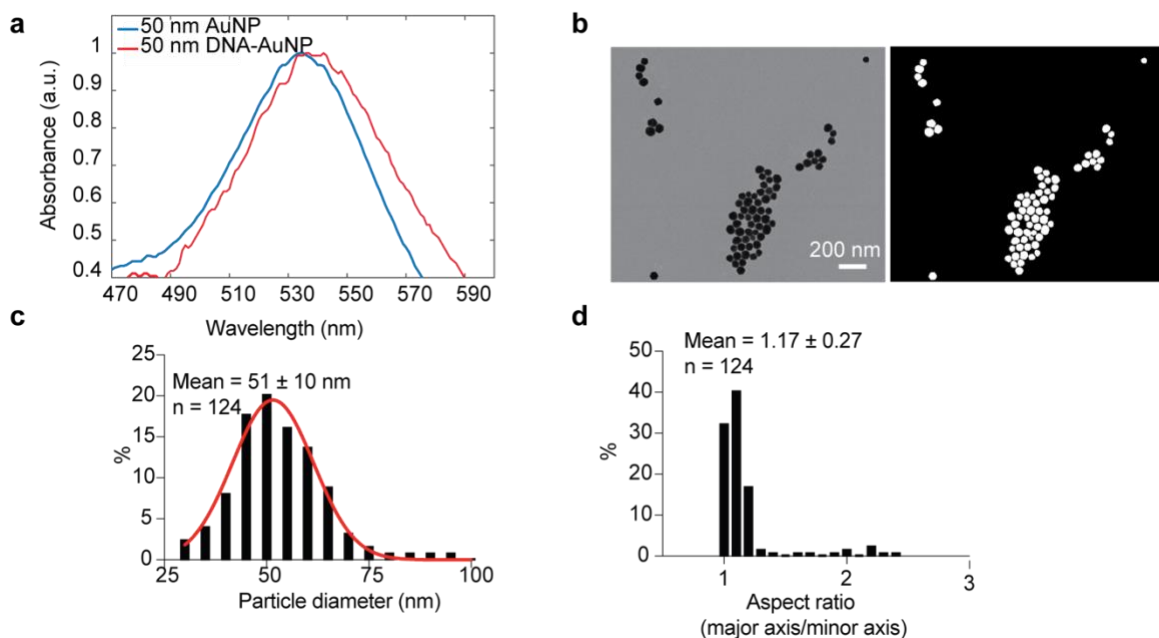
Figure S5. UV-VIS and TEM analyses of 50 nm DNA-AuNPs. (a) UV-VIS absorbance of 50 nm gold particles shows a red shift after DNA functionalization. (b) Raw TEM image along with thresholding filter and inverted threshold image to automatically calculate the area of each nanoparticle. (c) Histogram plot of particle diameters calculated from automated area measurement and assuming each nanoparticle was circular. (d) A histogram plot showing the distribution of aspect ratios of individual particles.

Structure	DNA leg / structure	surface area (μm^2)	DNA density ($1/\mu m^2$)
50 nm DNA-AuNP	1500 ± 50	7.85x 10^{-3}	1.9x 10^5
13 nm DNA-AuNP	107 ± 4	5.3 x 10^{-4}	1.9x 10^5
10 x40 nm DNA-AuNR	250 ± 16	1.3 x 10^{-3}	1.9x 10^5
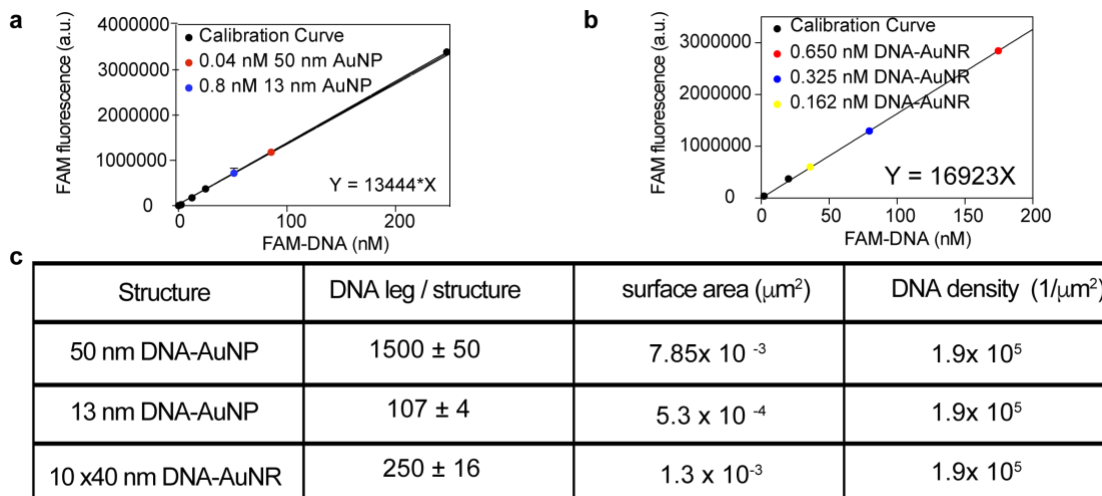
Figure S6. Quantification of DNA leg density for the structures used in this study. (a) Plot of FAM fluorescence used for quantification of density of spherical particles and AuNRs. The colored points show the intensities of the dissolved nanoparticle solutions and the derived concentrations of [FAM-DNA leg] from the calibration curves. (b). Please note that the calibration curves are different experiments conducted in different concentrations. (c) Table summarizing the results of these measurements. The error represents the standard error of the mean from triplicate measurements.

a

inset

RICM Movie

Inverted RICM Movie

Background subtracted
Inverted RICM Movie
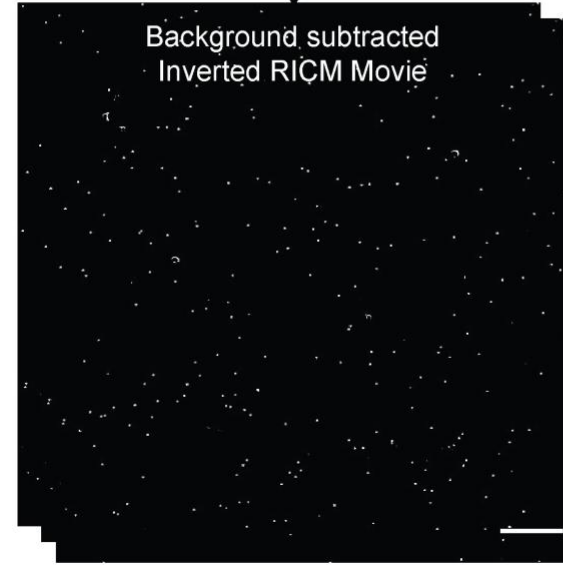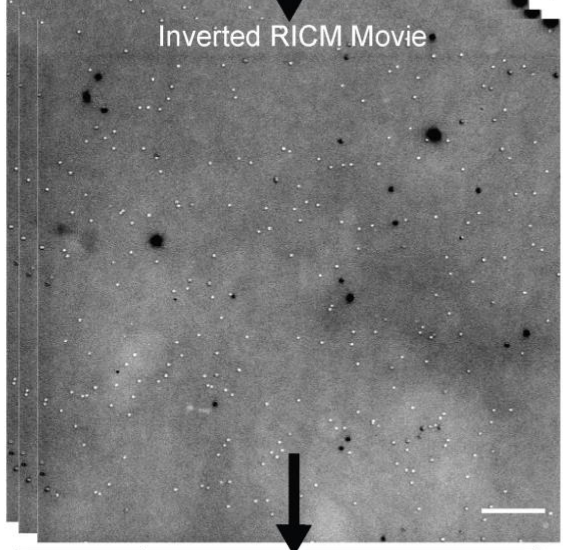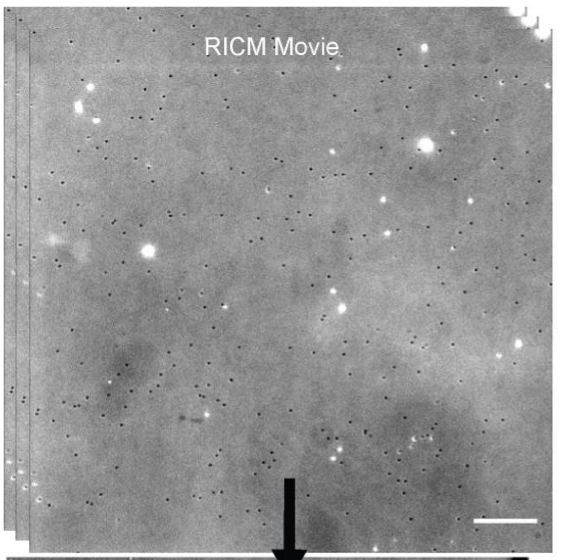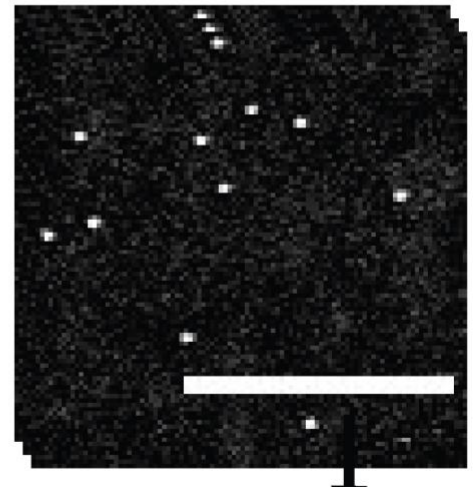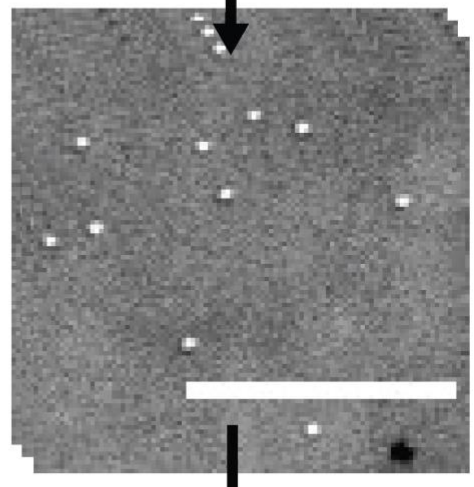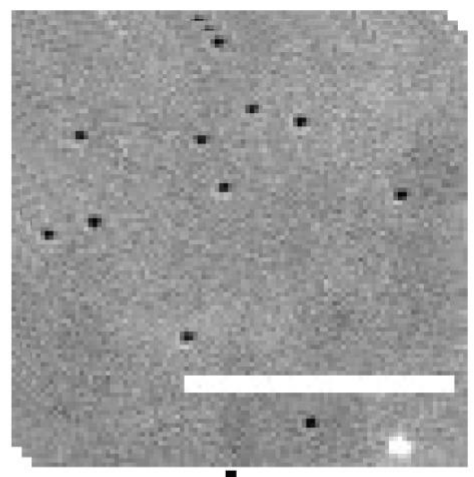
MOSAIC particle tracking
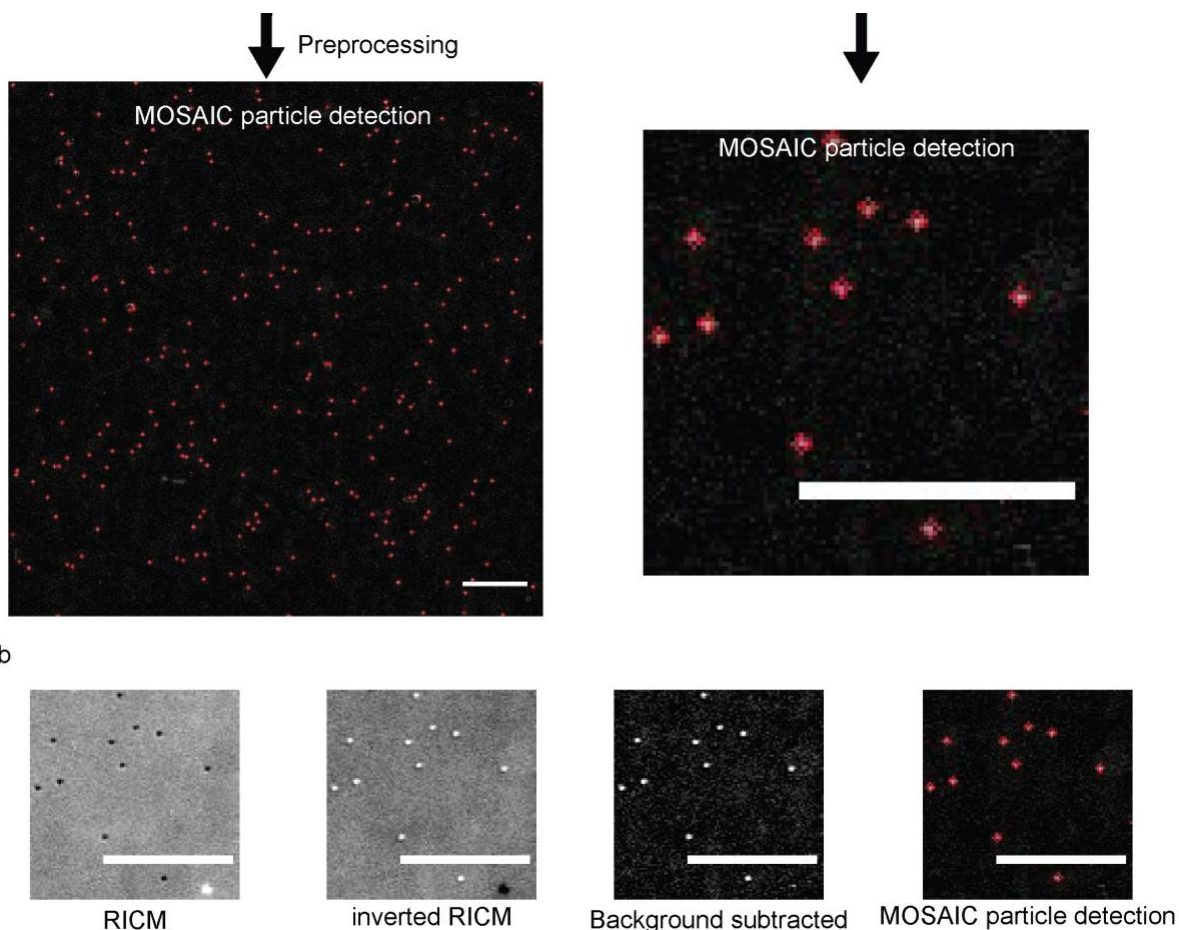
Figure S7. Localization of 50 nm DNA-AuNP motors based on scattering of the gold particle *via* the MOSAIC toolbox particle tracker[5]. The MOSAIC algorithm was used for particle detection as it showed high accuracy and precision and provides sub-pixel accuracy. (a) The flowchart for acquiring locations of 50 nm particles based on RICM signal. A large region of interest (left, scale bar = 10 μm) and an inset (right, scale bar = 5 μm) is shown for each step. The RICM image is first inverted so that nanoparticles appear as bright puncta. The inverted RICM time-lapse is then background subtracted. This step provides a high S/N for individual nanoparticles in addition to omitting nanoparticle aggregates from the RICM movie. Then, using the MOSAIC particle tracking software, the centroid locations of individual bright puncta in the background subtracted inverted RICM movie are extracted (the red outlines show detected particles in MOSAIC). The MOSAIC software automatically clusters these locations into trajectories and clustered trajectories are then exported to MATLAB for further analyses (Figure S11-S14). (b) The insets brought in (a) highlighting the precision and quality of particle tracking using this method. The red outlines show detected particles in MOSAIC. Scale bar is 5 μm.
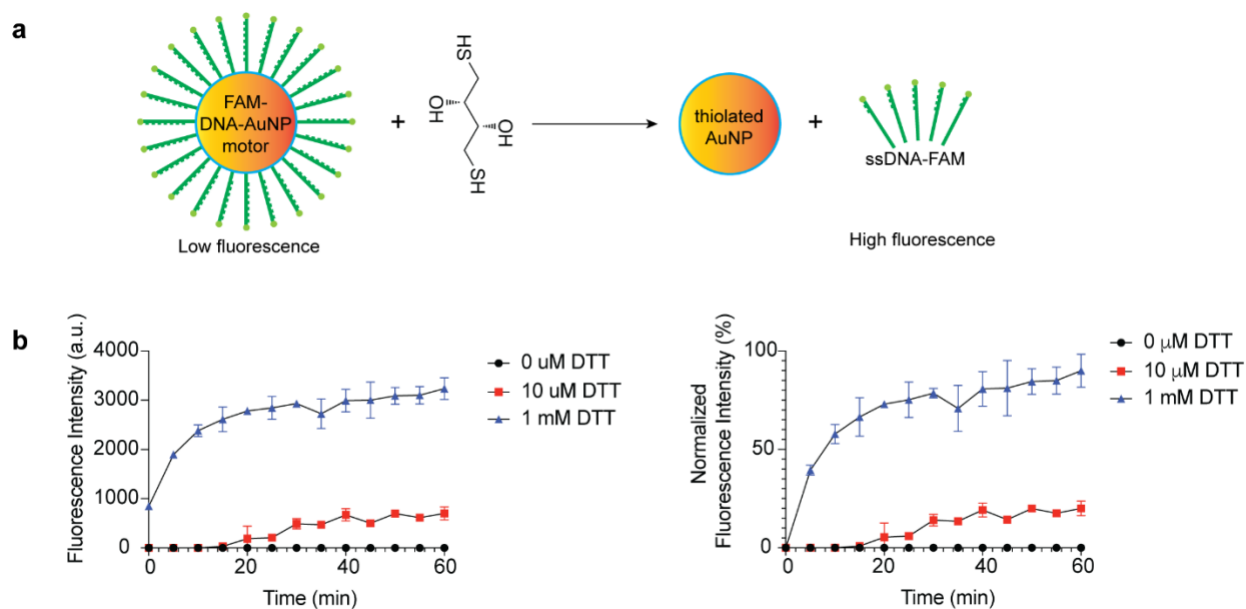
Figure S8. Stability of thiolated DNA-AuNPs in presence of 10 μM and 1 mM DTT, 10% formamide, 0.75% Triton X and 1X RNase H buffer. (a) Schematic of the reaction used to test the stability of the DNA motors. (b) Plot of fluorescence *vs* time (left) and normalized fluorescence *vs* time (right) in the presence of 10 μM and 1 mM DTT. Experiments on the surface were conducted in the presence of 10 μM DTT.
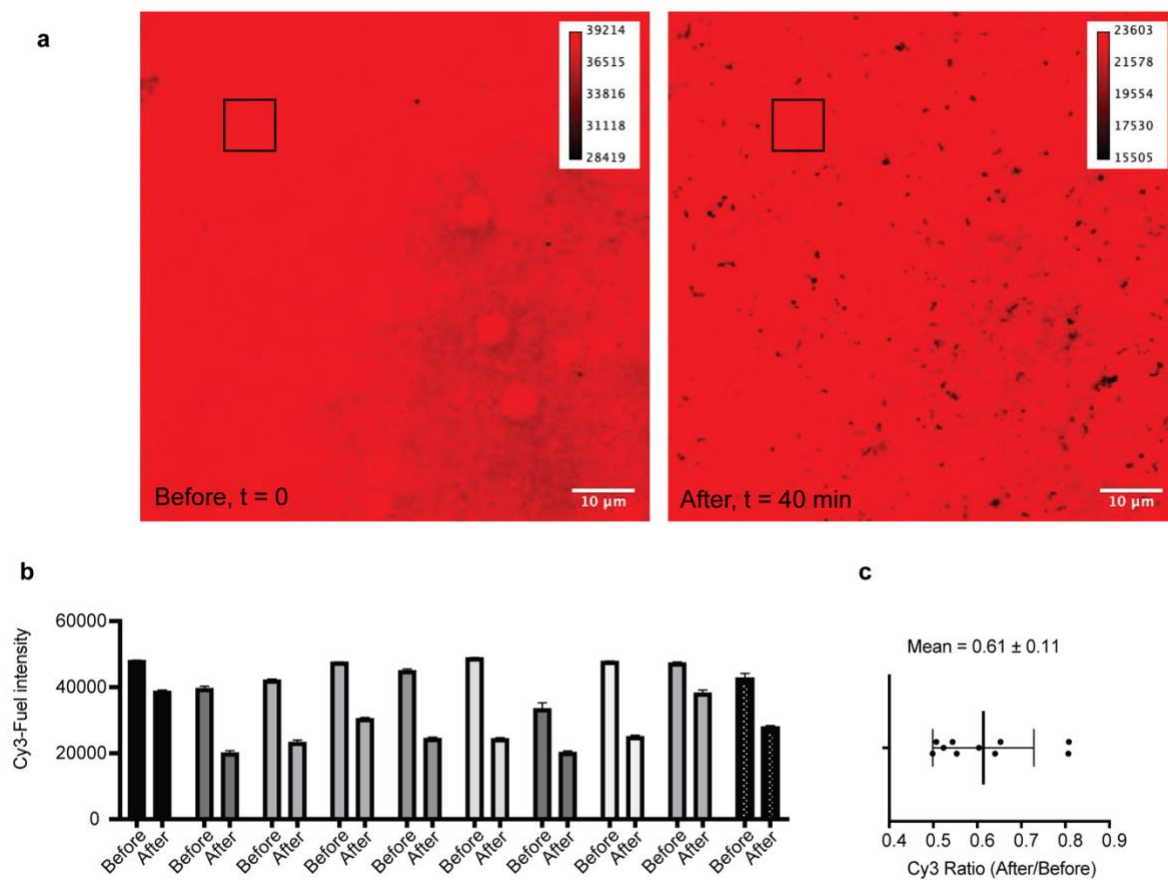
Figure S9. Non-specific RNA degradation. (a) Representative Cy3 images before and after a 35-minute rolling acquisition in RICM. "After" images were taken at t = 40 min after initiating rolling by addition of RNase H. A region (such as the black square) on the surface without depletion tracks is selected to ensure we are studying the effect of non-specific cleavage. Fluorescence intensity is measured before and after acquisition. (b) Comparison of before and after intensities on 10 different surfaces and acquisitions. (c) Distribution of ratios of (after/before) Cy3-fuel intensities shows that on average 40% of RNA fuel is lost due to non-specific hydrolysis.
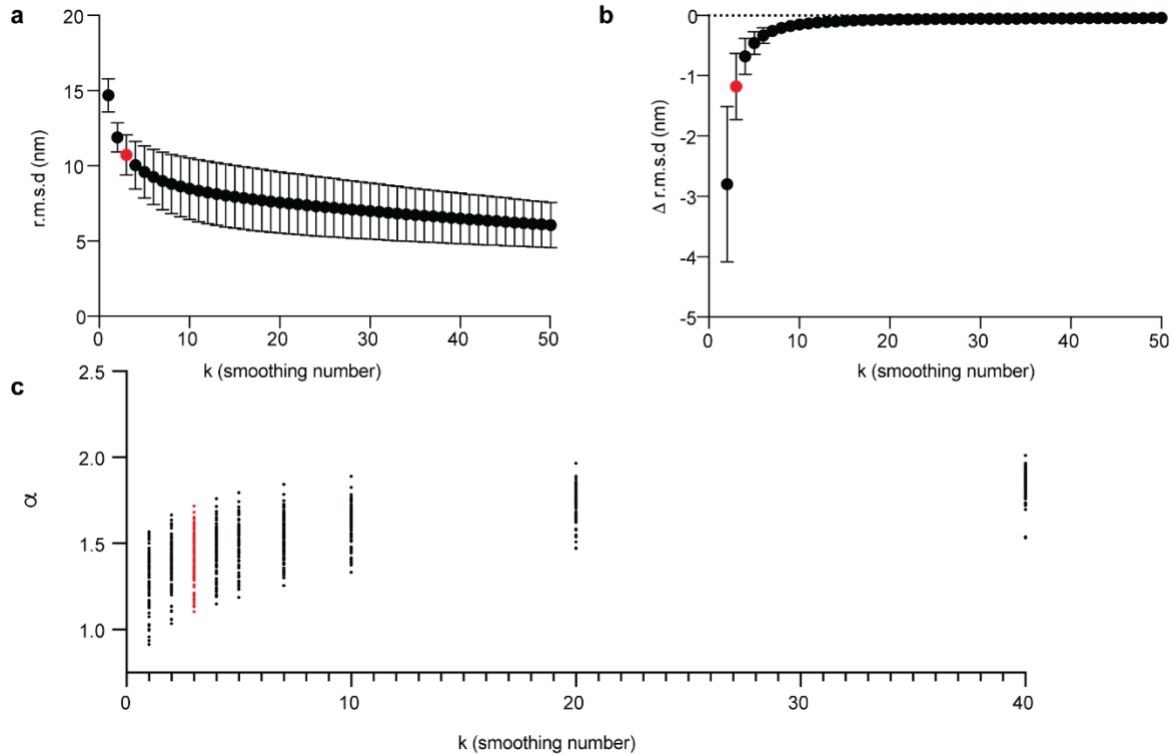
Figure S10. Effect of smoothing of trajectories on root mean squared displacement (r.m.s.d.) of negative controls. (a) Plot of average r.m.s.d. of trajectories of motors in the absence of RNase H as a function of smoothing number (k). Each dot represents the mean of trajectories (a total of 903 trajectories) from 3 independent experiments. Error bars represent the standard deviation of r.m.s.d. between the three experiments. (b) The first derivative of plot in (a) shows error reduction as a function of smoothing number k. This plot shows that most of the localization error is averaged out by a smoothing number of 3. (c) A plot of α as a function of smoothing number k for motors moving in the presence of 30 nM RNase H. This plot shows that using a high smoothing number increases the apparent increase in the α values. Hence, we smoothed all trajectories using a moving average of 3 consecutive points, as this point shows a balance between efficiently reducing localization error (a-b) and minimally changing the observed dynamics.
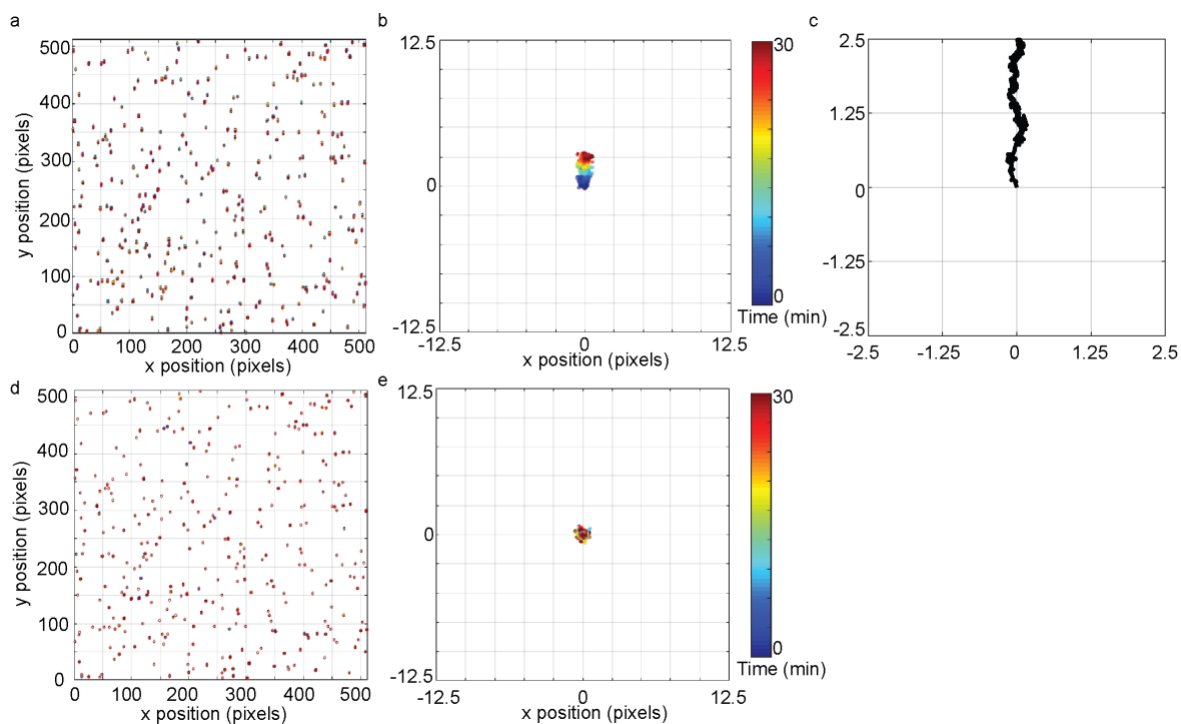
Figure S11. Drift correction of negative control. (a) Raw localization outputs from MOSAIC tool suite (1 pixel = 160 nm). (b) All trajectories plotted by setting the start position at the center of coordinate system. (c) A plot of average drift calculated using velocity correlation. This average drift is subtracted from all trajectories to correct for drift. (d) Drift corrected localizations and (e) plotted from the center. Here we specifically chose to show an experiment with high drift to highlight the robustness of the drift correction algorithm.
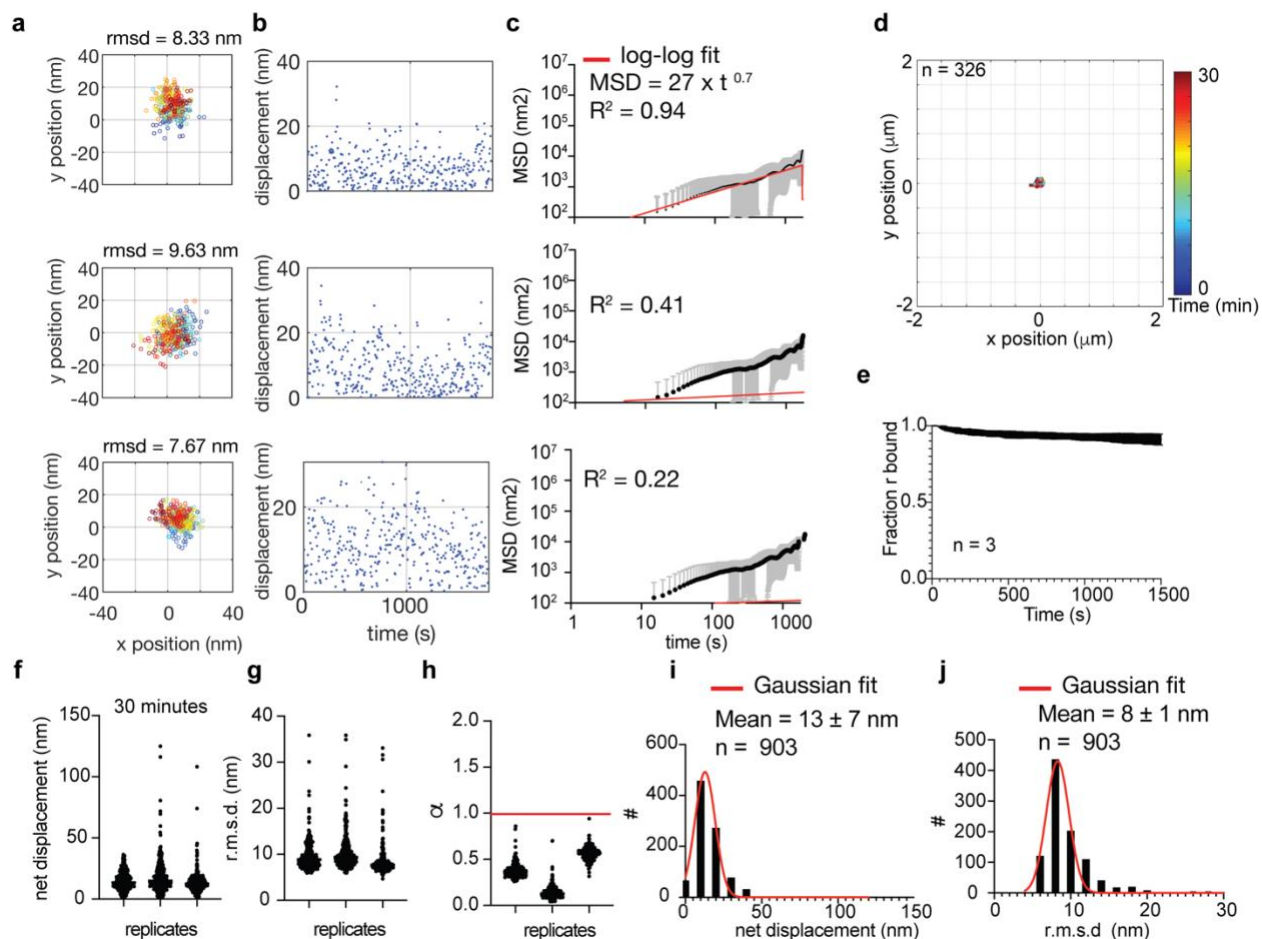
Figure S12. Ensemble analyses of DNA-AuNP motors without the addition of RNase H. DNA-AuNP motors remain immobile due to DNA/RNA hybridization (a) Precision of DNA-AuNP localization. Three representative trajectories are shown. The precision of localization is measured by calculating the root mean squared displacement (r.m.s.d) of each particle. (b) Plot of displacement *vs* time. Each blue dot shows the displacement of a particle shown in (a) from its initial position at t = 0. (c) Plot of MSD *vs* log-lag-time for stalled motors. Black dots show the mean MSD for each lag time and error bars represent the standard deviation. The red line indicates the log-log fit from which the α value is derived. This fit usually results in a very low R^2 for stalled particles. In the cases that $R^2> 0.9$ the α value is always below one. (d) Trajectories of 326 particles plotted from the center and color coded by time. (e) Plot of fraction bound *vs* time from 3 independent experiments shows that motors remain bound to the surface without the addition of RNase H. (f) Plot of net displacements and (g) average root mean squared displacement (r.m.s.d.) and (h) α value for stalled motors in three replicates. Each dot represents a single motor at each replicate. The red line in h is drawn to show that motors without RNase H have α <1. (i) Histogram of net displacements and (j), r.m.s.d for *n* = 903 motors without addition of RNase H. In each histogram the mean and standard deviation is approximated by a Gaussian fit to the histogram indicated by a red line.
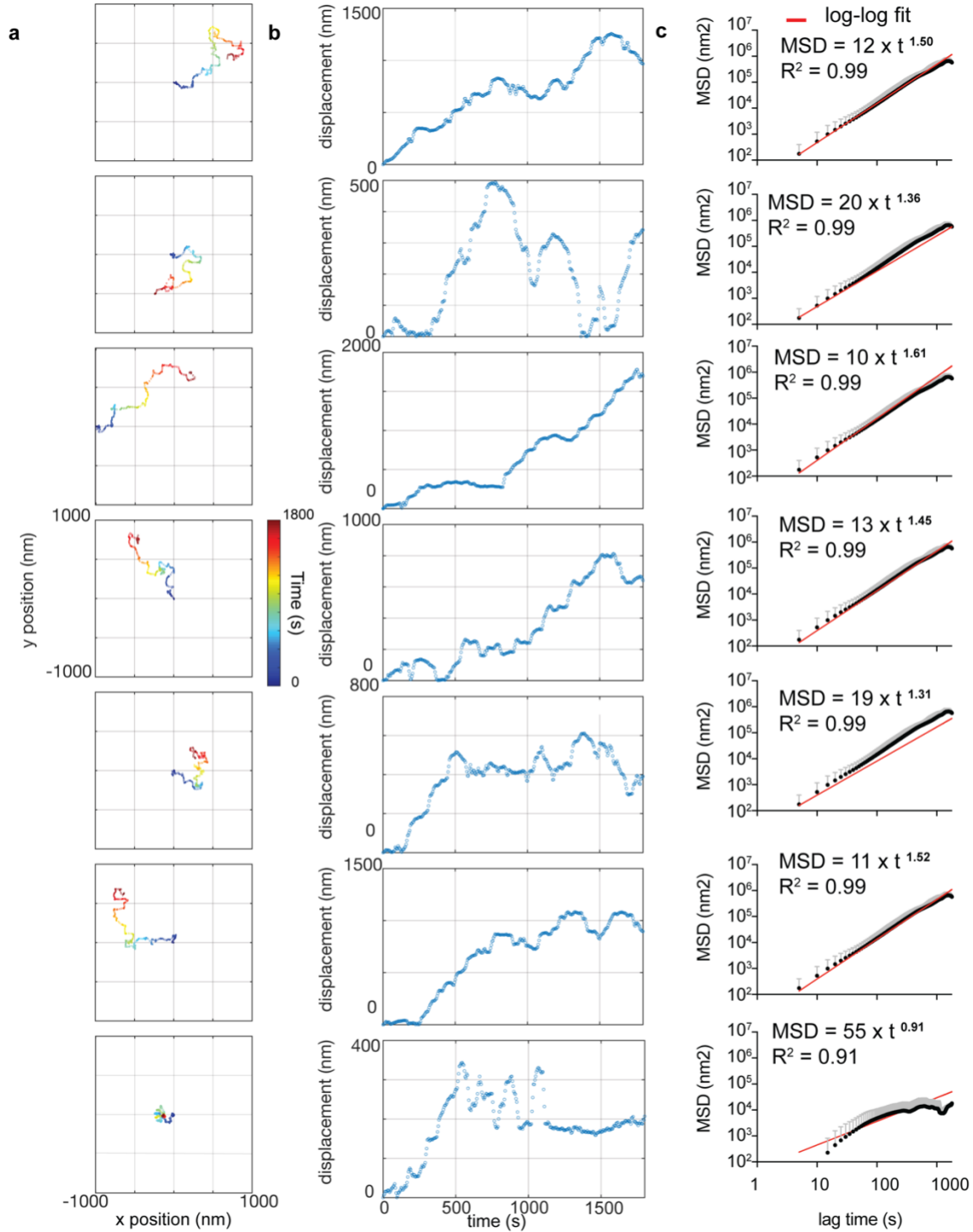
21

Figure S13. Individual track analyses of 7 motors in the presence of 30 nM RNase H. (a) Trajectories of motors plotted from the center of coordinates in a 2x2 μm box. Each dot represents the location of a single motor, color coded by time. (b) Plot of displacement *vs* time. Each blue dot shows the displacement of the particle from its initial position at t = 0. (c) Plot of log MSD *vs* log-lag time for each motor. Black dots show the mean MSD for each lag time and error bars represent the upper standard deviation. The red line indicates the log-log fit from which the α value is derived.
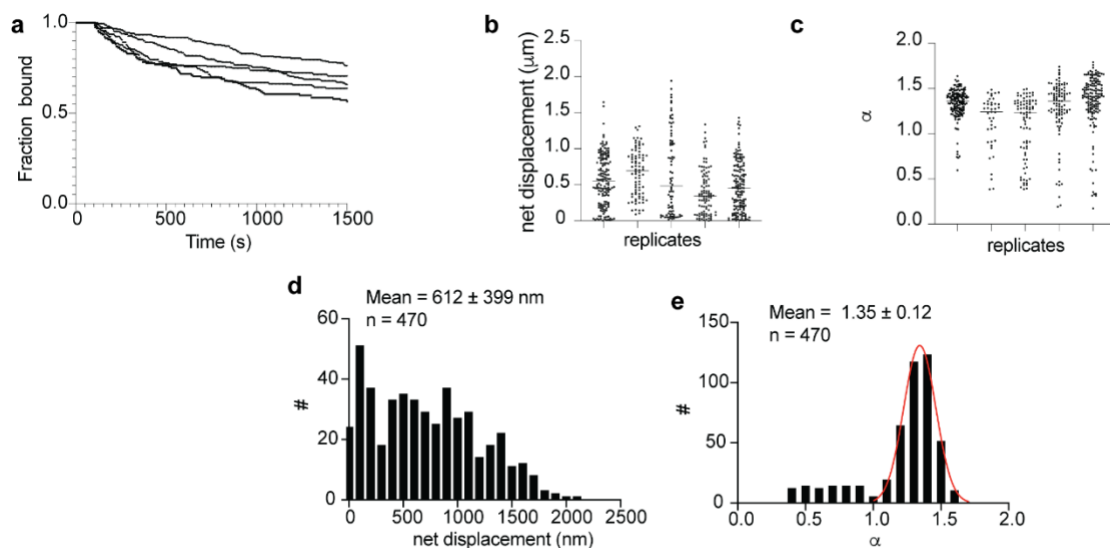
Figure S14. Ensemble analyses of 50 nm AuNPs in the presence of 30 nM RNase H. (a) Plot of fraction bound *vs* time from 5 independent experiments. Two additional replicates are included in this SI figure to show the robustness of the experiment. (b) Plot of net displacements in 30 minutes, (c) α values for 5 replicate experiments. (d) Histogram of net displacements in 30 minutes and (e) α values of 470 motors generated from 5 independent experiments in the presence of 30 nM RNase H. The mean and standard deviation for net displacements is derived from the raw data while for α is approximated by a Gaussian fit to the histogram at (α >1) indicated in red.
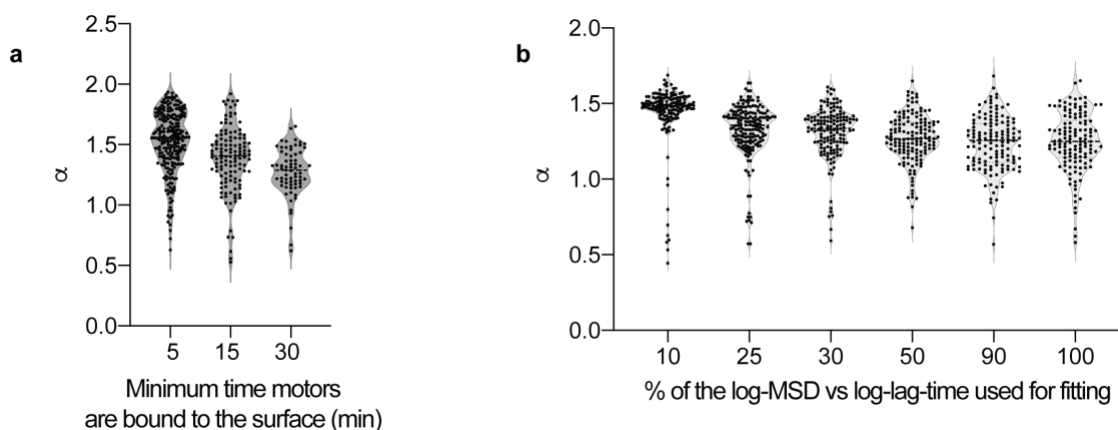
Figure S15. Measuring α as a function of trajectory length and fraction of log-MSD *vs* log-lag-time curve to be included in the fit. (a) Measuring α as a function of minimum time required for motors to be analyzed. Analyses of all tracks in (a) use 100% of the log-MSD *vs* log-lag time plot to yield an α (due to the low number of MSD points in 5-minute sample). This plot shows that α for shorter tracks is higher before dissociation. (b) plot of α as a function of % of the log-MSD *vs* log-lag time used for log-log fitting. We used 25 % for tracking 30-minute rolling acquisitions for the remainder of this study as it offers a high number of MSD points for each lag-time as well as capturing the dynamic of the system.
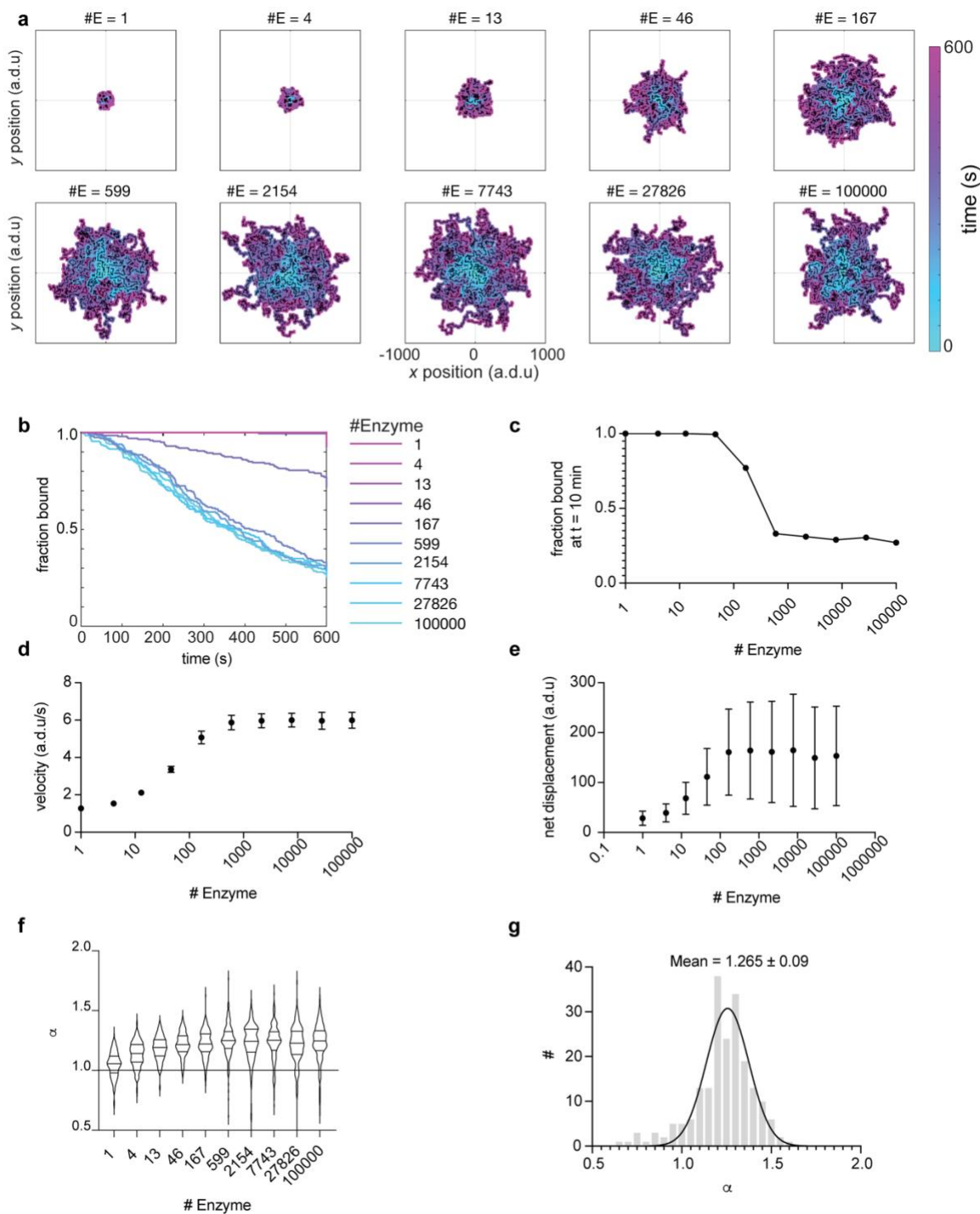
Figure S16. Simulation results investigating the effect of enzyme concentration on motor performance. (a) Simulated trajectories of motors plotted from the center of coordinates with different number of enzyme molecules introduced in the simulation. Each condition contains 200 trajectories plotted from the center of the coordinates and color-coded by time. (b) Plot of fraction of motors bound to surface as a function of time. Dissociation is defined as all DNA legs occupying the unbound condition in the simulation. (c) Plot of fraction of motors bound at $t = 10$

minutes (end of simulation). This plot shows that increasing the enzyme molecules available to a motor decreases processivity. (d) plot of velocities and (e) net displacement for motors as a function of number of enzyme molecules. Each dot represents the mean of 200 simulated tracks at each condition. Error bars represent the standard deviation. (f) Plot of α values as a function of number of enzyme molecules. The distribution of α values are demonstrated as violin plots where the median and quartiles are indicated by horizontal lines. (g) a histogram of α values at #E = 100,000. The mean is approximated with a Gaussian fit to the histogram (black line).
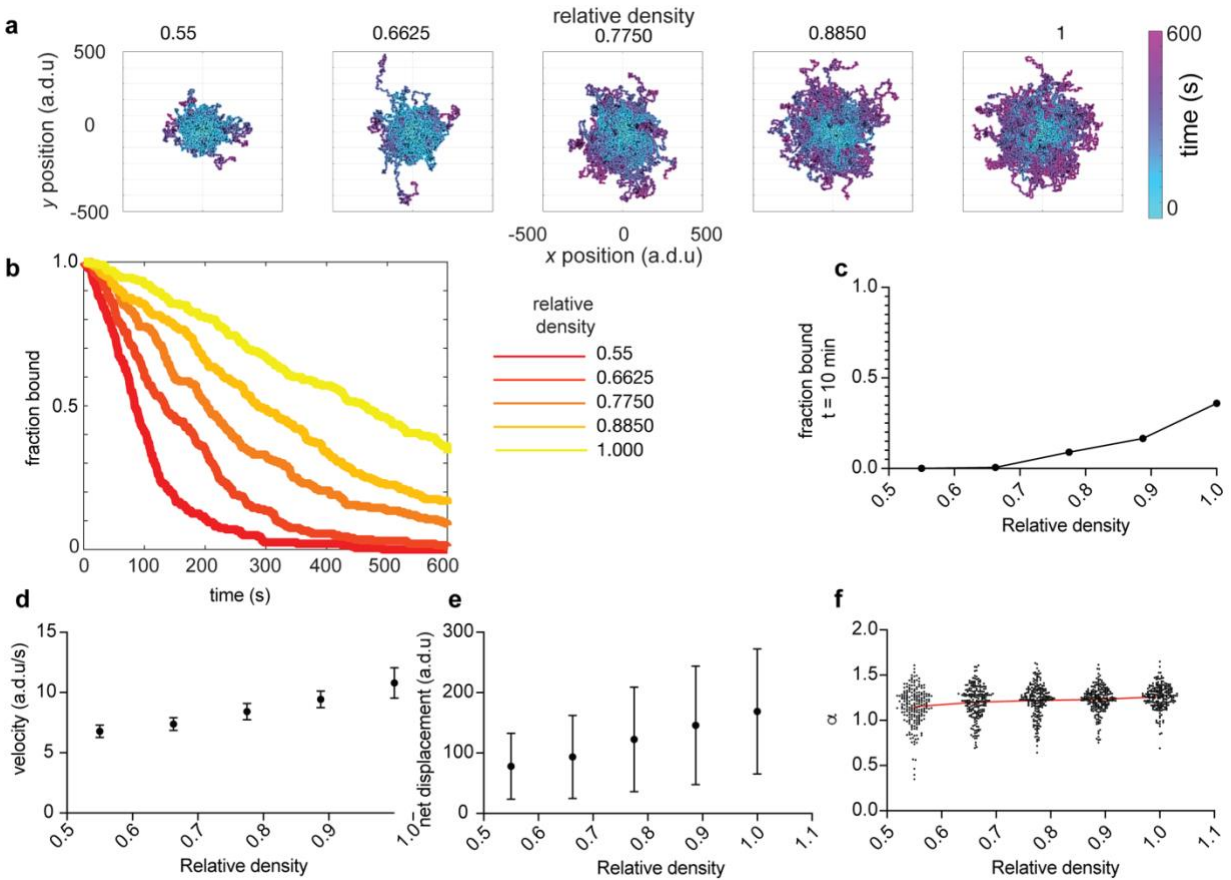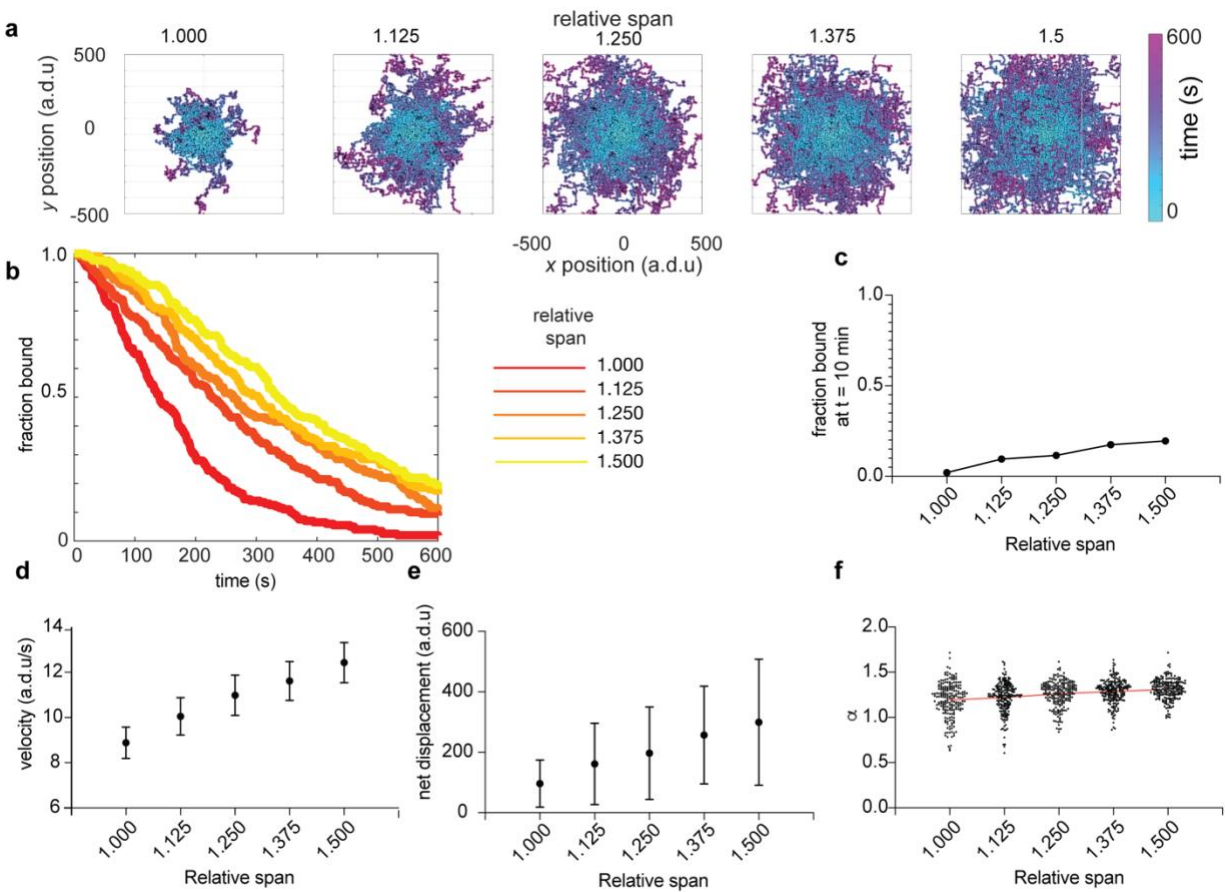
Figure S17. Simulation results investigating effect of DNA leg density on motor performance. (a) Simulated trajectories of 200 simulated motors plotted from the center of coordinates with different density of DNA legs introduced in the simulation. For this simulation we used a high enzyme number to be able to investigate the role of density in processivity and speed. Trajectories are color-coded by time. (b) Plot of fraction of motors bound to surface as a function of time. Dissociation is defined as all DNA legs occupying the unbound condition in the simulation. (c) Plot of fraction of motors bound at t = 10 minutes (end of simulation). This plot shows that increasing the density of DNA legs of a motor increases processivity. (d) Plot of velocities and (e) net displacement for motors as a function of relative DNA density. Each dot represents the mean of 200 simulated tracks at each condition. Error bars represent the standard deviation. (f) Plot of a for motors as a function of relative DNA density. Each dot represents the a for a single motor. Red line connects the means of each condition.
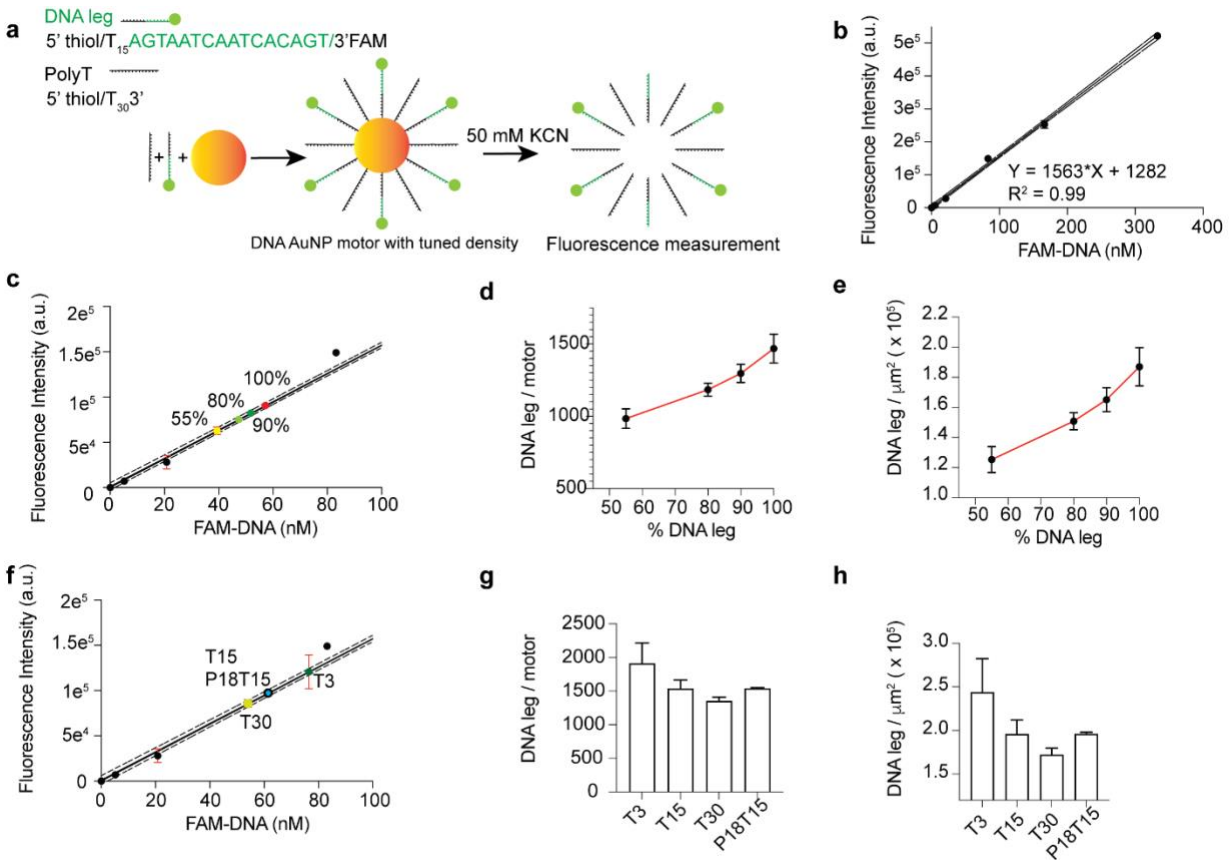
Figure S18. Fluorescence calibration curve used to determine DNA leg density per motor.
(a) Schematic of the reaction used to measure density of DNA legs in DNA motors with tuned density. (b) Calibration curve used for measurements. (c) Inset of the calibration curve alongside tuned density AuNP motors. Colored dots show individual samples. (d) By dividing the DNA concentration extracted from calibration curve and the AuNP concentration of each sample (40 pM) # DNA leg / motor is defined. (e) The density of DNA on each motor is calculated by dividing #DNA legs/ surface area of nanoparticles ($4 \times 3.14 \times (25)^2 = 7850$ nm^2 = 0.00785 μm^2). (f) Inset of the calibration curve alongside dissolved AuNP with different span. Colored dots show individual samples. (g) By dividing the DNA concentration extracted from calibration curve and the AuNP concentration of each sample (40 pM) # DNA leg / motor is defined (h) The density of DNA on each motor is calculated by dividing #DNA legs/ surface area of nanoparticles ($4 \times 3.14 \times (25)^2 = 7850$ nm^2 = 0.00785 μm^2).

Figure S19. Simulation results investigating the effect of DNA leg span on motor performance. (a) Simulated trajectories of motors plotted from the center of coordinates with different density of DNA legs introduced in the simulation. For this simulation we used a high enzyme concentration to be able to investigate the role of span in processivity and speed. Each condition contains 200 trajectories plotted from the center of the coordinates and color-coded by time. (b) Plot of fraction of motors bound to surface as a function of time. Dissociation is defined as all DNA legs occupying the unbound condition in the simulation. (c) Plot of fraction of motors bound at t = 10 minutes (end of simulation). This plot shows that increasing the span of DNA legs of a motor increases processivity. (d) plot of velocities and (e) net displacement for motors as a relative span. Each dot represents the mean of 200 simulated tracks at each condition. Error bars represent the standard deviation. (f) Plot of a for motors as a function of relative span. Each dot represents the a for a single motor. Red line connects the means of each condition.
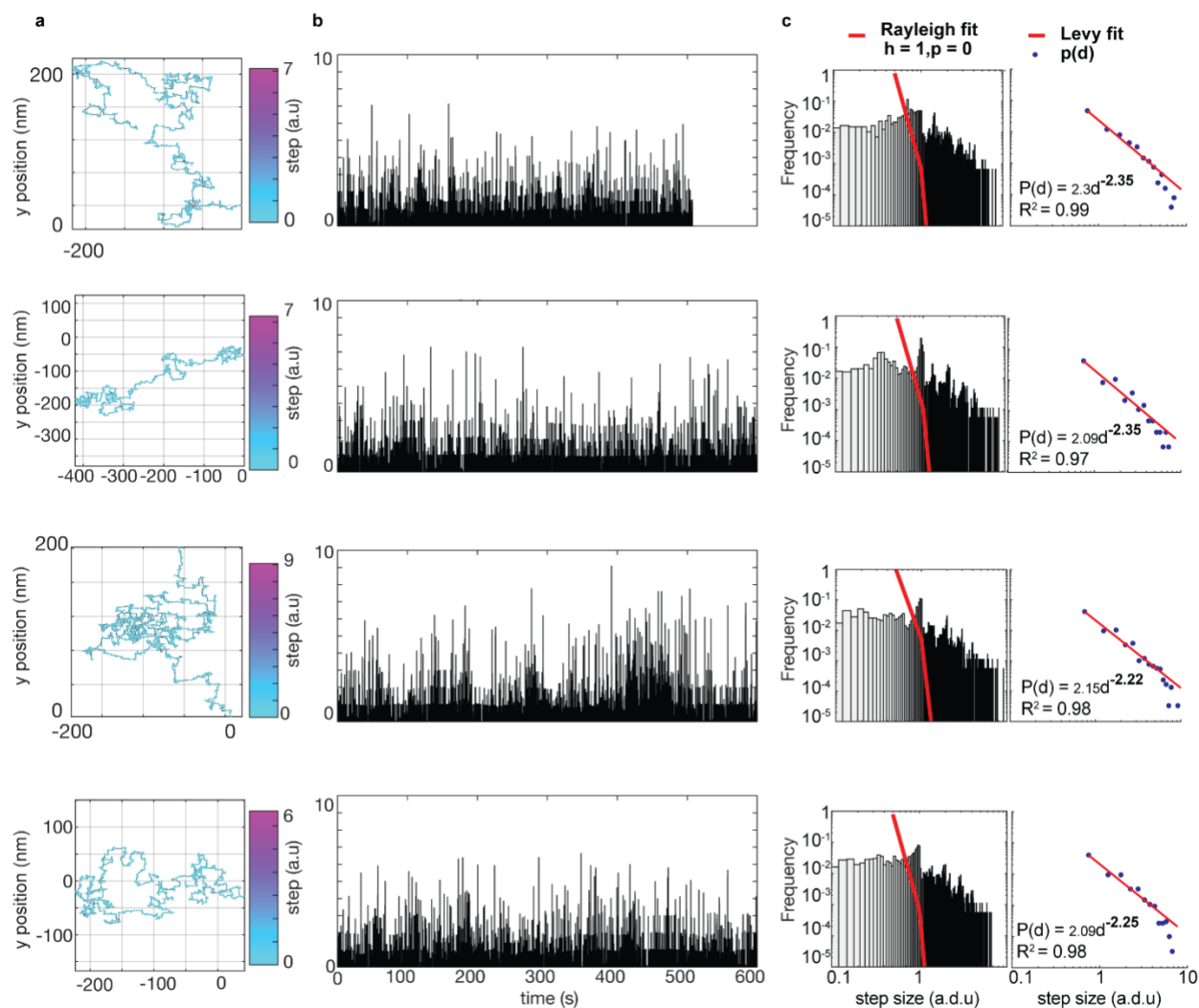
Figure S20. Simulated motors exhibit Levy type motion. (a) Trajectory of four simulated motors with high density, high span at high enzyme number (100,000). (b) Plot of step size *vs* time shows that step size is heterogeneous and fluctuates over time. (c) Probability density function of step sizes with the Rayleigh fit (red) super imposed. The *h* and *p* value of the Kolmogorov-Smirnov test (ks-test) shows that the Rayleigh distribution is a poor fit for the data primarily as a result of the high probability of observing large step size (step size >1). (d) Probability distribution of motor step size shown only for step size > 1 (blue dots). The red line represents a power law fit super-imposed on the data. The power law coefficient was used to infer the Levy coefficient. The heavy tail of the probability distribution of simulated tracks is well described by a Levy fit ($R^2 > 0.95$).
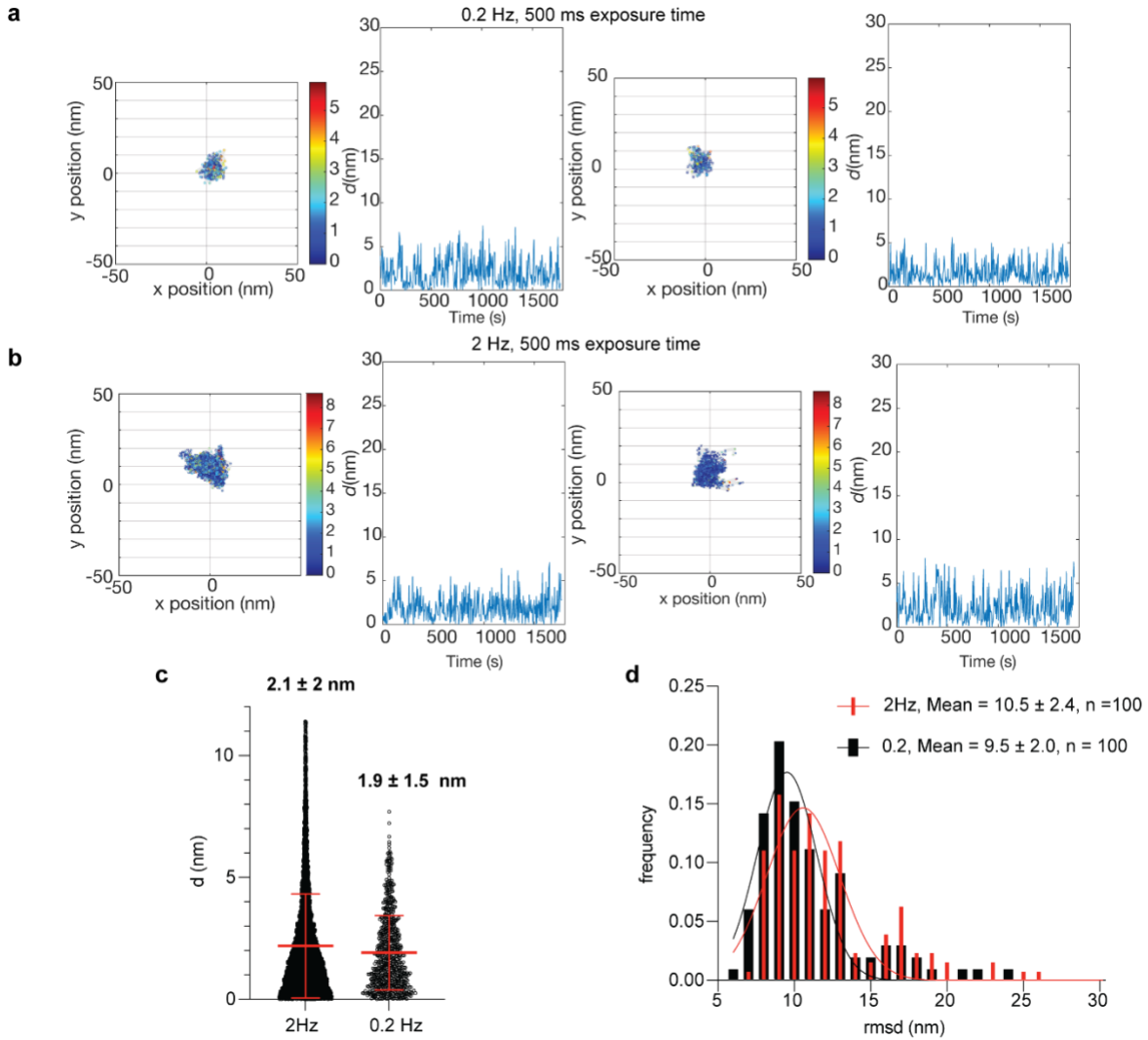
Figure S21. Effect of imaging frequency on particle localization precision. Representative trajectories and plots of step size *vs* time for single particles imaged with 500 ms exposure time at 0.2 Hz (a) and 2 Hz (b) imaging rate. (c) Plot of step size *d vs* imaging rate acquired using 500 ms exposure time. Each dot shows a single *d* value obtained from 10 trajectories. There are 36,000 values for the 2 Hz measurement and 3600 values for the 0.2Hz of measurements. The horizontal line shows the mean and the error bars show the standard deviation. (d) A histogram of rmsd for 100 motors imaged with 500 ms exposure time at 0.2 and 2Hz. The mean rmsd is approximated by a Gaussian fit to the distribution.
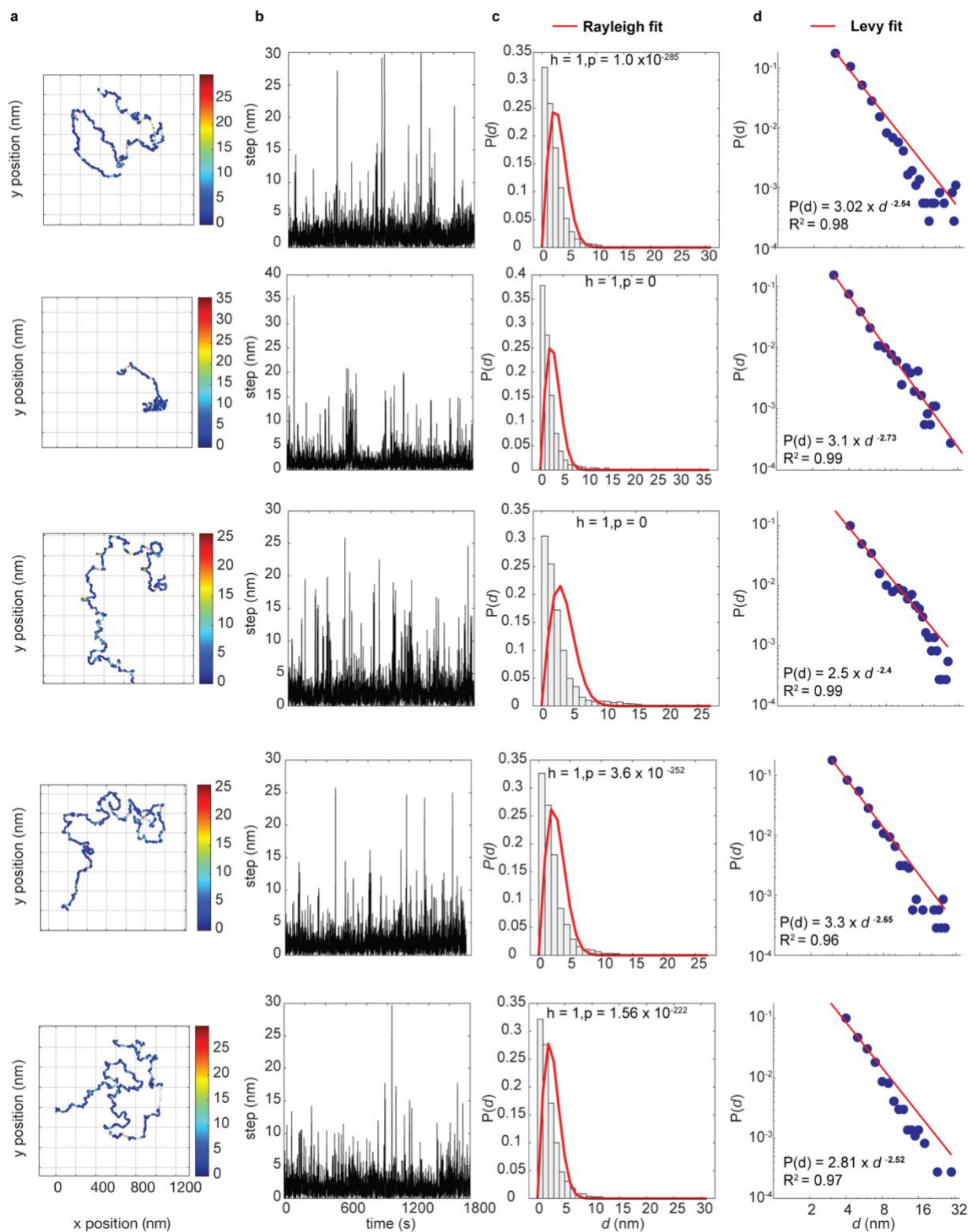
Figure S22. AuNP motors exhibit Levy type motion. (a) Trajectory of five AuNP motors moving in the presence of 30 nM RNase H **(b)** Plot of step size *vs* time shows that step size is heterogeneous and fluctuates over time. **(c)** Probability density function of step sizes with the

Rayleigh fit (red) super imposed. The *h* and *p*-value of the Kolmogorov-Smirnov test (ks-test) shows that the Rayleigh distribution is a poor fit for the data (d) Probability distribution of motor step size shown only for step size > 4 nm (blue dots). The red line represents a power law fit super-imposed on the data. The power law coefficient was used to infer the Levy coefficient. The heavy tail of the probability distribution of simulated tracks is well described by a Levy fit (R^2> 0.95).
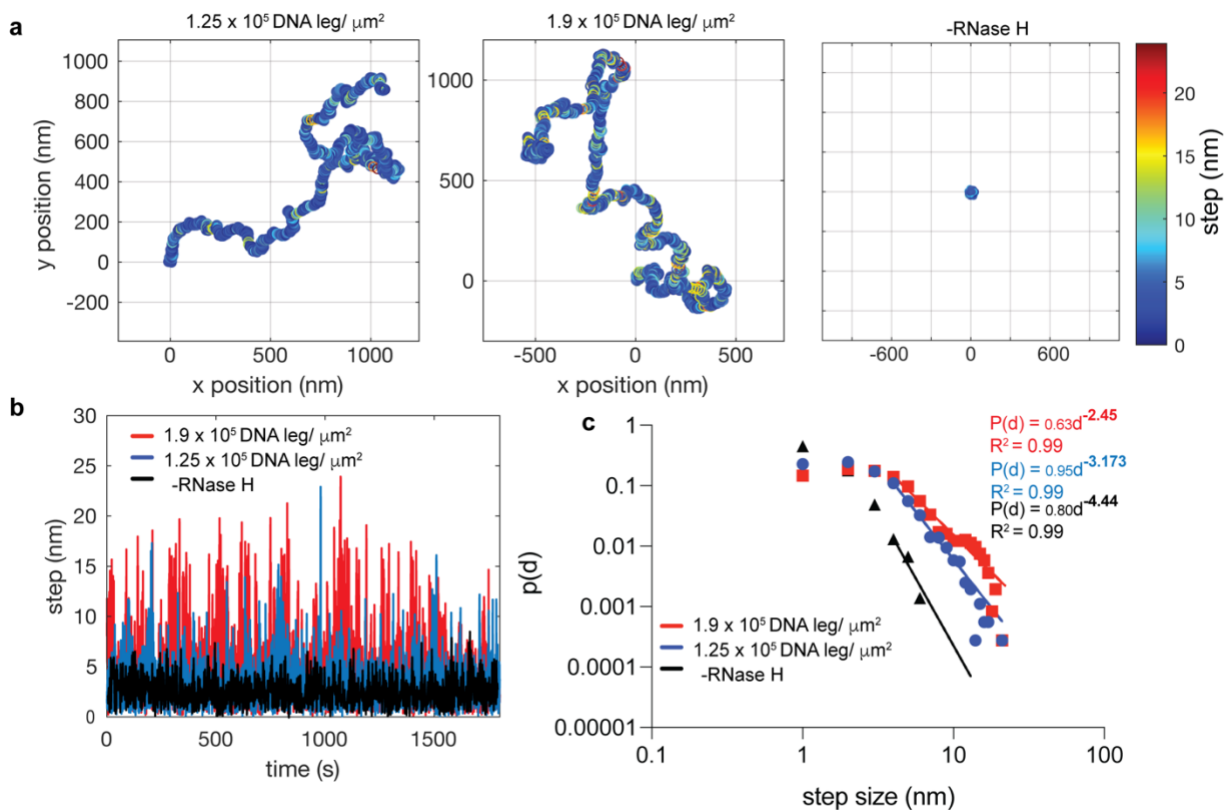
Figure S23. Increasing DNA leg density increases the probability of high-speed bursts. (a) Trajectories of 3 DNA-AuNP nanomotors imaged for 30 minutes and color-coded by their step sizes. (b) Plot of step sizes *vs* time for these 3 motors. High DNA leg density motor takes more frequent large steps. (c) This increase in probability of fast steps is shown by the decrease in the Levy coefficient μ.
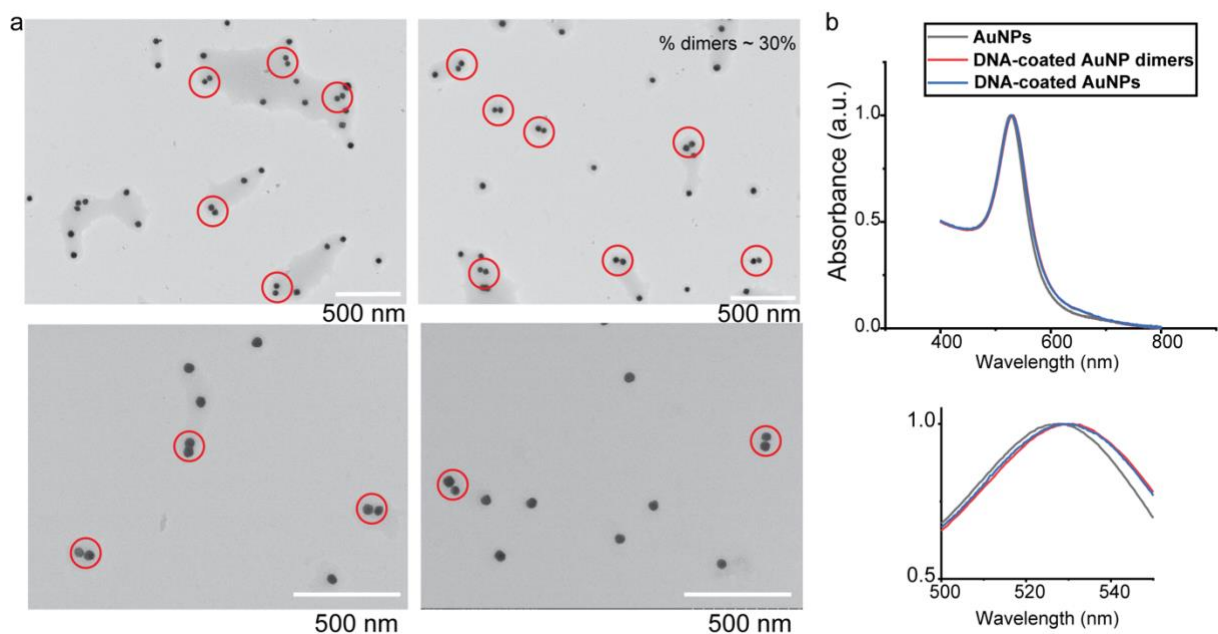
Figure S24. TEM and UV characterization of AuNP dimers. (a) TEM images of AuNP dimerized particles. (b) UV absorbance spectra comparing AuNPs, DNA coated AuNPs and DNA coated AuNP dimers. A slight red shift is observed in the dimer enriched DNA-coated AuNPs.
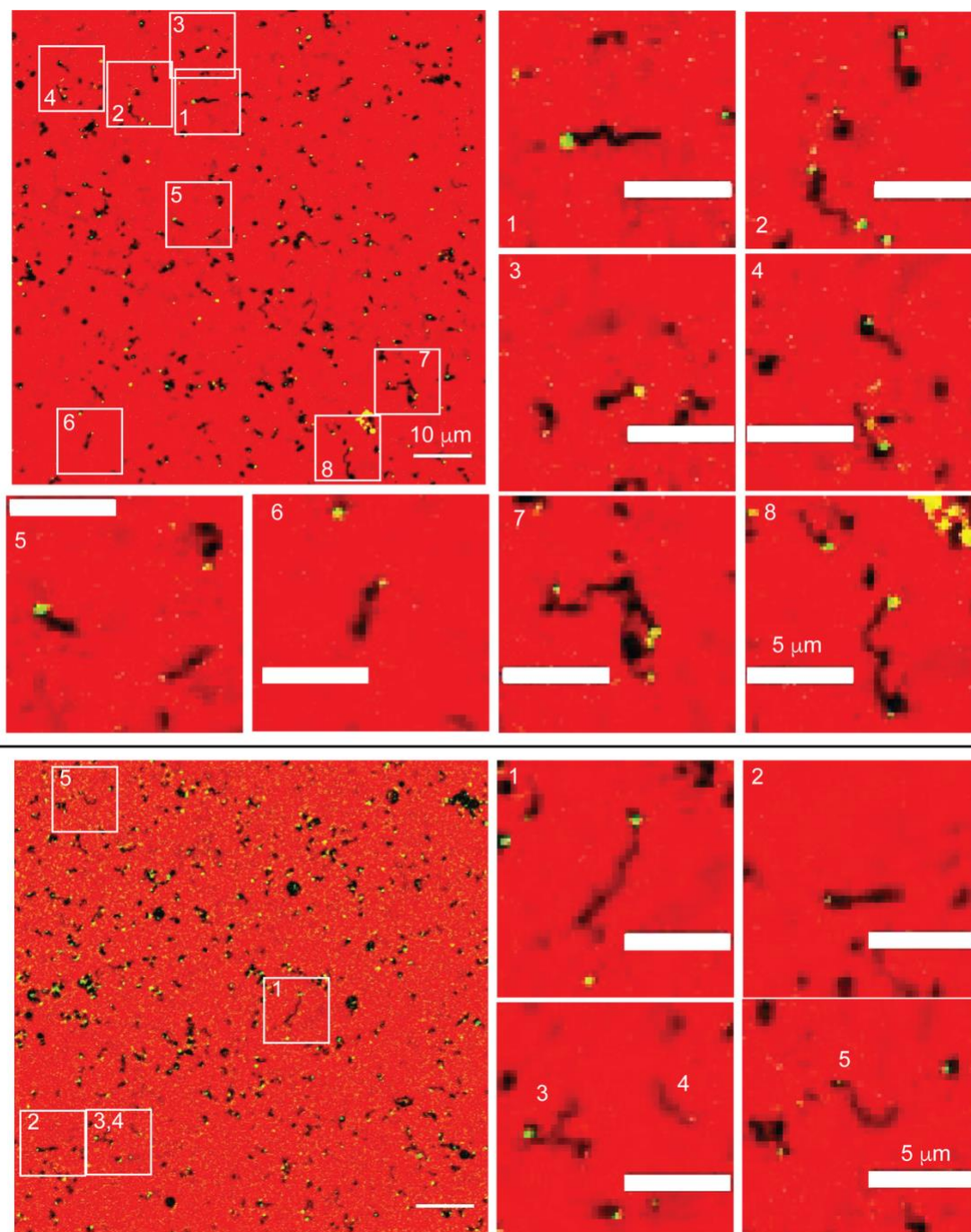
Figure S25. Widefield images of 50 nm dimer depleted tracks. FAM AuNP motor is colored green while Cy3-RNA fuel is colored red. From two ROIs, tracks that have a long linear trajectory are highlighted. Images in the two channels were acquired at t = 1 hour after addition of 30 nM RNase H in 1X RNase H buffer, 10% formamide and 0.75% triton X. Inset scale bars are 5 μm.
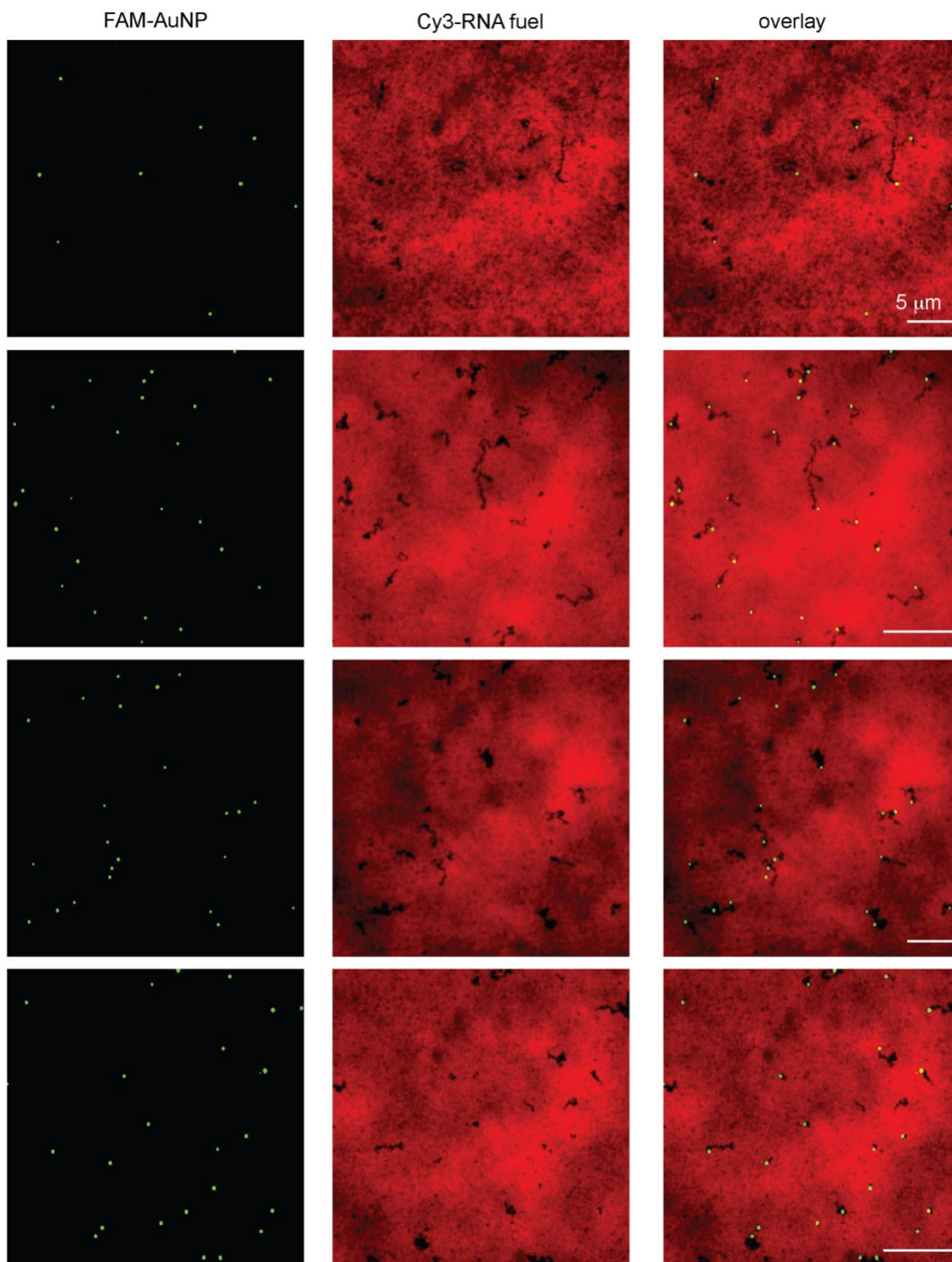
Figure S26. Representative SIM images of 50 nm dimer enriched AuNP motors. FAM AuNP motor is colored green while Cy3-RNA fuel is colored red. Microfluidic wells were washed with 2 mL of 100 mM $MgCl_2$ to stop the reaction at t = 1 hour after addition of 30 nM RNase H in 1X RNase H buffer, 10% formamide and 0.75% triton X. The microfluidic wells

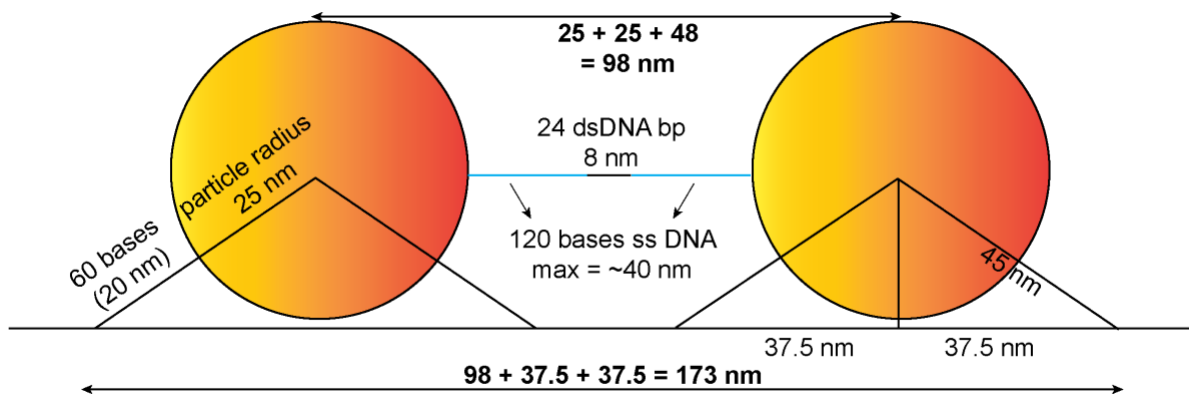were incubated in 100 mM MgCl$_2$ overnight and imaged using a SIM microscope in FAM and Cy3 channels the next morning.

Figure S27. A simple geometric model for chemically ligated DNA 50 nm gold nanoparticle dimers. The strands for dimerization are brought in table S1.
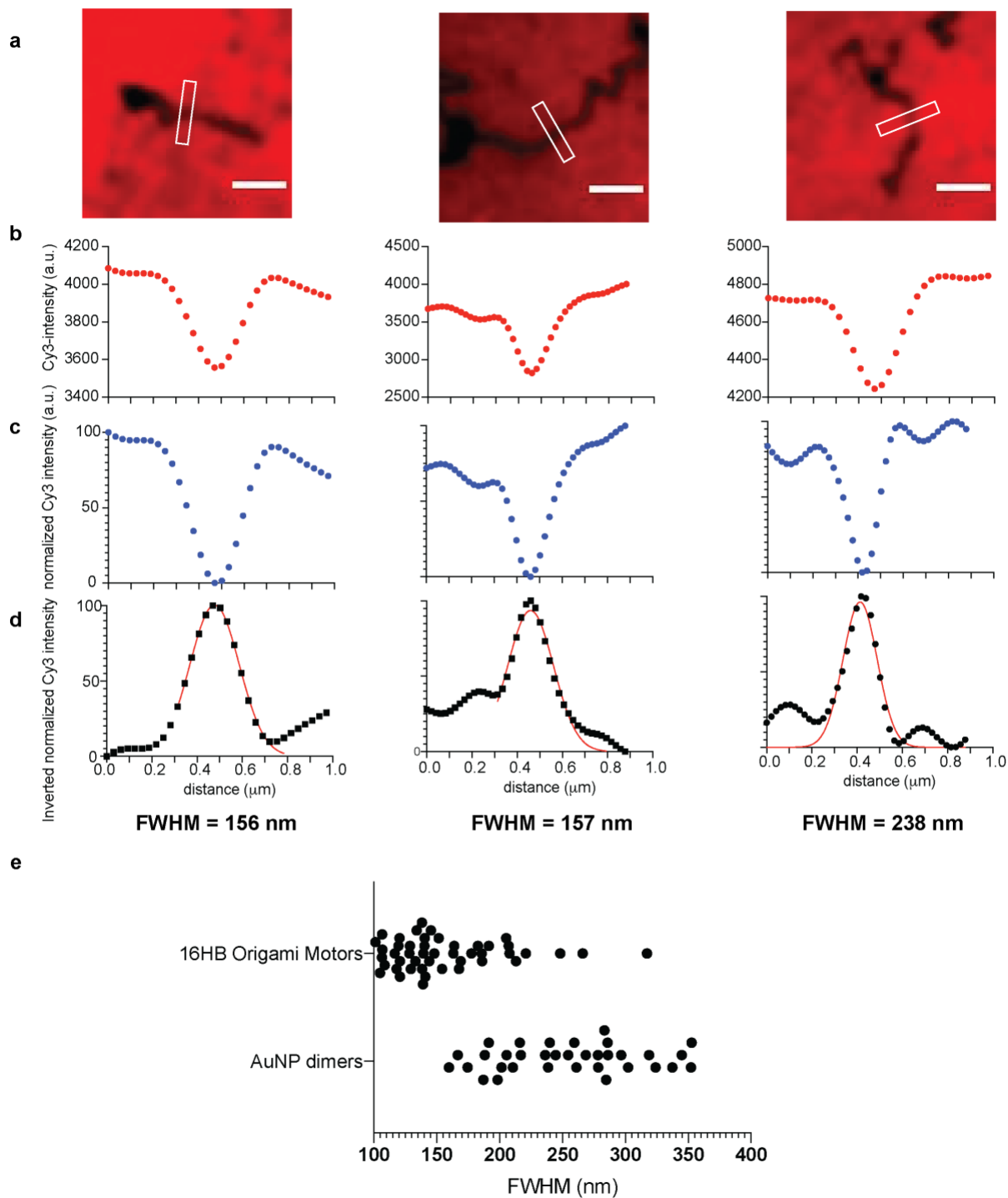
Figure S28. SIM track width analyses. (a) Representative linear tracks found in SIM images and showing a linescan of width = 5 pixels drawn perpendicular to motor direction. Scale bar is 1 μm. (b) Representative linescans of individual tracks. (c) Normalized intensity values were plotted in blue and (d) while red shows the Gaussian fit to the inverted fluorescence linescans. (e) Plot of Full Width at Half Maximum (FWHM) of 34 AuNP dimer tracks using SIM. FWHM

are calculated by fitting the normalized inverted fluorescence values to $f(x) = a1 * \exp(-((x-b1)/c1)^2)$ then the full width at half maximum is defined as FWHM= (f.c1/1.4142) * 2.355 * 1000. Plot of FWHMs for 16HB DNA origami motors is brought to show that the reported 150 nm is above the resolution obtained by SIM and the minimum is reported as a dimer track width. Note that measuring track width for monomer spherical motors is unattainable due to rapid direction change of motor at scales below the optical resolution of SIM.
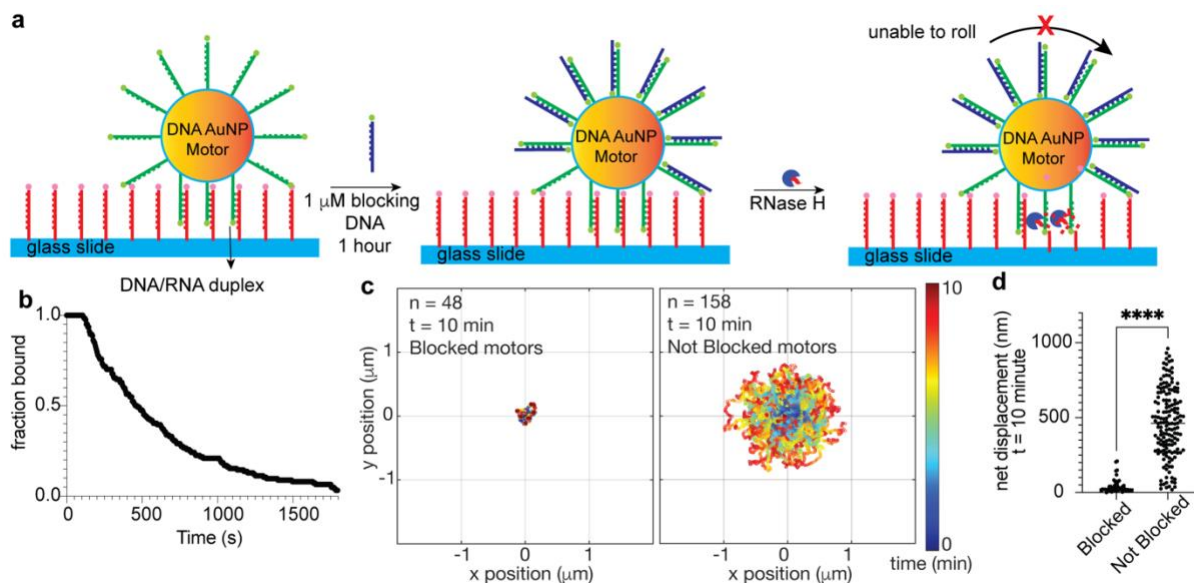
Figure S29. Blocking the DNA above the particle leads to rapid dissociation and minimal translocation of DNA-AuNP motors. (a) schematic to generate motors that are unable to roll. After hybridization of DNA-AuNP to the RNA monolayer a short blocking DNA that is complementary to the DNA legs is added at a high concentration. After washing excess blocking DNA and addition of 30 nM RNase, motors are expected to either slide to translocate or dissociate. (b) Calculation of fraction of motors bound as a function of time shows motors dissociate rapidly from the surface. Almost all motors dissociated during the 30-minute acquisition. (c) Trajectories of motors bound to the surface at t = 10 minutes. Left shows 48 blocked motors and right shows 158 motors that are not blocked (d) A plot of net displacements of blocked and not blocked motors. Blocked motors exhibit minimal motion, thus confirming rolling as a primary mechanism for motor motion. Each dot represents the net displacement for a single motor and **** represents p<0.0001.

Table S1. Oligonucleotide sequences used in this study. Table summarizing the sequences of oligonucleotides and their naming system. The sequences are displayed in a 5' to 3' orientation. The 3' and 5' and internal, DNA and RNA modifications indicated in table S1 are illustrated in table S2.

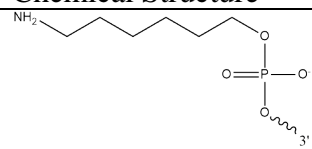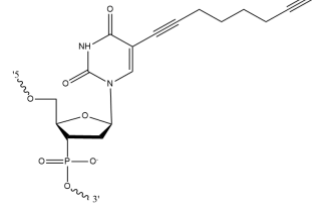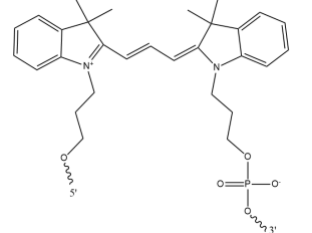| ID	Sequence (5'-3')
DNA anchor	5'-AmMC6/GA GAG AGA TGG GTG CTT TTT TTT TTT TTT T/3'-5OctdU/
RNA/DNA chimera substrate[1]	GCACCCATCTCTCTCrCrCrCrCrCrCrCrUrGrUrGrArUrUrGrArUrUrArCrU /3'-Cy3Sp/
DNA leg (T15)[2]	/5'-ThioMC6-D/TT TTT TTT TTT TTT TAG TAA TCA ATC ACA GT/3'-6-FAM/
DNA leg (T3)	/5'-ThioMC6-D/ TTT AG TAA TCA ATC ACA GT/3'-6-FAM/
DNA leg (T30)	/5'-ThioMC6-D/ TTTTTTTTT TTTTTTTTTTTTTTTTTTTTT AG TAA TCA ATC ACA GT/3'-6-FAM/
PolyT	/5'-ThioMC6-D/ TTT TTT TTT TTT TTT TTT TTT TTT TTT TTT
Blocking DNA	CTGTGATTGATTACT
Linker strand 1[3]	5'-ThioMC6-D /TTTGGCCGAGGACTCCTGCTCCGCTGCGGTTTGGCGAACTGGACCGTCTACTTA CCGTT TCCGACGAGCCACA-**M1**-CCGGAACAGCCC
Linker strand 2[4]	5'-ThioMC6-D /TTTCGCGCACCTGAGACCTTCTAATAGGGTTTGCGACAGTCGACGACTAGAATGC CCTTTGGGCTGTTCCGGA-**M2**-GTGGCTCGTCGG

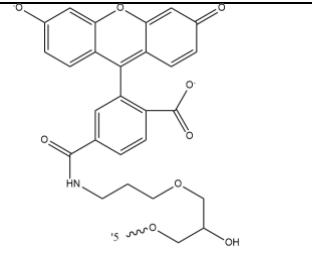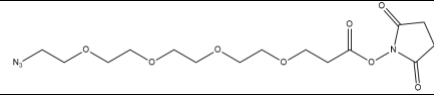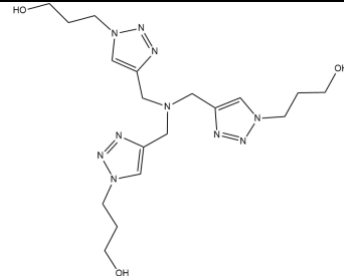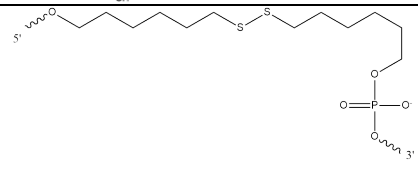[1] Red bases indicate RNA bases in the RNA/DNA chimeric molecule.
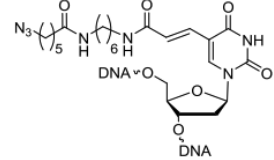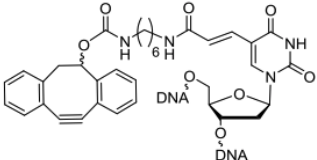
[2] Green colored bases indicate the RNA binding portion of the DNA legs.

[3] M1 indicates an internal azide modification (see table S2)

[4] M2 indicates an internal alkyne modification (see table S2)

Table S2. Chemical structure of DNA and RNA modifications and surface modifications used in this study.

Modification ID	Modification name	Chemical Structure
5'-AmMC6	5' Amino modifier C6	
3'-5OctdU	3' 5-Octadiynyl dU	
3'-Cy3Sp	3'Cy3™ fluorescent dye	
3'-6-FAM	Fluorescein	
NP4A	NHS peg 4 azide	
THTPA ligand		
5'-ThioMC6-D	5' Thiol Modifier C6 S-S	

M1	Internal Azide modification	
M2	Internal alkyne modification	

References:

1. Liu, B.; Liu, J., Freezing Directed Construction of Bio/Nano Interfaces: Reagentless Conjugation, Denser Spherical Nucleic Acids, and Better Nanoflares. *Journal of the American Chemical Society* **2017,** *139* (28), 9471-9474.

2. Bastus, N. G.; Comenge, J.; Puntes, V., Kinetically Controlled Seeded Growth Synthesis of Citrate-Stabilized Gold Nanoparticles of up to 200 nm: Size Focusing *versus* Ostwald Ripening. *Langmuir* **2011,** *27* (17), 11098-11105.

3. Liu, B. W.; Liu, J. W., Freezing Directed Construction of Bio/Nano Interfaces: Reagentless Conjugation, Denser Spherical Nucleic Acids, and Better Nanoflares. *J Am Chem Soc* **2017,** *139* (28), 9471-9474.

4. Bazrafshan, A.; Meyer, T. A.; Su, H.; Brockman, J. M.; Blanchard, A. T.; Piranej, S.; Duan, Y.; Ke, Y.; Salaita, K., Tunable DNA Origami Motors Translocate Ballistically over μm Distances at nm/s Speeds. *Angewandte Chemie International Edition* **2020,** *59* (24), 9514-9521.

5. Sbalzarini, I. F.; Koumoutsakos, P., Feature Point Tracking and Trajectory Analysis for Video Imaging in Cell Biology. *Journal of Structural Biology* **2005,** *151* (2), 182-195.

6. Tarantino, N.; Tinevez, J.-Y.; Crowell, E. F.; Boisson, B.; Henriques, R.; Mhlanga, M.; Agou, F.; Israël, A.; Laplantine, E., TNF and IL-1 Exhibit Distinct Ubiquitin Requirements for Inducing NEMO–IKK Supramolecular Structures. *Journal of Cell Biology* **2014,** *204* (2), 231-245.